Advanced Approaches Applied to Photovoltaic Power Generation for System Reliability and Resilience

XUAN JIAO

Doctor of Philosophy (Engineering)

THE UNIVERSITY OF SYDNEY

Supervisor: A/Prof.Weidong Xiao
Associate Supervisor: Dr.Sinan Li

A thesis submitted in fulfilment of
the requirements for the degree of
Doctor of Philosophy

School of Electrical & Information Engineering
Faculty of Engineering
The University of Sydney
Australia

25 October 2024

Statement of Originality and Scholarship

This is to certify that to the best of my knowledge, the content of this thesis is my own work. This thesis has not been submitted for any degree or other purposes.

I certify that the intellectual content of this thesis is the product of my own work and that all the assistance received in preparing this thesis and sources have been acknowledged.

I acknowledge that I received the Univerisity of Sydney Tuition Fee Scholarship to cover my fees in the third year of my PhD course study from 1st January 2023.

Authorship Attribution Statement

The thesis contains material that I have previously published during my PhD study.

Chapter 2 of this thesis is published as

- **X. Jiao**, T. Yang, X. Li, S. Ding and W. Xiao, "A DC Side Power Ramp Rate Control Strategy for High Performance and Low Cost PV Systems," in CPSS Transactions on Power Electronics and Applications, vol. 8, no. 2, pp. 128-136, June 2023, doi: 10.24295/CPSSTPEA.2023.00013.

Chapter 3 of this thesis is published as

- **X. Jiao**, X. Li, D. Lin and W. Xiao, "A Graph Neural Network Based Deep Learning Predictor for Spatio-Temporal Group Solar Irradiance Forecasting," in IEEE Transactions on Industrial Informatics, vol. 18, no. 9, pp. 6142-6149, Sept. 2022, doi: 10.1109/TII.2021.3133289.
- **X. Jiao**, X. Li, Z. Ge and W. Xiao, "A Predictive Power Ramp Rate Control Scheme with an Updating Gaussian Prediction Confidence Estimator for PV Systems,"in Solar Energy, vol. 276, pp. 112648, July 2024, doi: 10.1016/j.solener.2024.112648.

Chapter 4 of this thesis is published as

- **X. Jiao**, X. Li, Y. Yang and W. Xiao. "Novel and Comprehensive Approach for Power Loss Estimation of Soiled Photovoltaic Modules," in Solar Energy, vol. 268, pp. 112283, January 2024, doi: 10.1016/j.solener.2023.112283.

Chapter 5 of this thesis is published as

- **X. Jiao**, X. Li, T. Yang, Y. Yang and W. Xiao, "A Novel Fault Diagnosis Scheme for PV Plants Based on Real-Time System State Identification," in IEEE Journal of Photovoltaics, vol. 13, no. 4, pp. 571-579, July 2023,
doi: 10.1109/JPHOTOV.2023.3262950.

As the only first author, I have made a substantial contribution to the above journal papers including but not limited to designing the study, deriving mathematical equations, programming and modelling, analysing the data and writing the drafts of the manuscripts. In addition to the statements above, in cases where I am not the corresponding author of a published item, permission to include the published material has been granted.

Signature:

As supervisor for the candidature upon which this thesis is based, I can confirm that the authorship attribution statements above are correct.

Signature:

Abstract

This thesis presents a comprehensive analysis of challenges and recent advancements in solar photovoltaic (PV), focusing on enhancing solar energy system performance in terms of operational efficiency. It addresses explicitly interconnected issues within power ramp rate control (PRRC), soiling loss estimation, and fault detection and diagnosis—critical components for improving system performance. The contributions in each area are intricately linked to facilitate the seamless integration of PV systems with the power grid for efficient ancillary services.

Two chapters dedicated to PRRC explore innovative methods that collectively enhance the stability and responsiveness of solar power systems. The first chapter introduces a variable step-size power reserve control method that operates independently of BESS, proving its efficacy in managing PRRC more effectively than traditional methods. The second chapter builds on this by implementing a deep learning-based model to predict solar irradiance accurately, which is crucial for precise and advanced ramp rate control. This model integrates with an optimization-based control method to achieve real-time, low-complexity PRRC, showcasing a significant improvement in managing the fluctuations caused by environmental factors such as cloud cover and soiling.

The thesis also delves into soiling loss estimation, where a hybrid approach using image processing and circuit modelling is proposed to predict power losses due to soiling accurately. This estimation is vital for adjusting the PRRC strategies, as soiling can mimic shading effects similar to cloud cover, affecting the solar output and complicating the ramp rate control. By accurately predicting soiling losses, the system can differentiate between actual cloud-induced shading and soiling, enabling more precise control adjustments and better integration with BESS for peak shaving and load levelling.

Moreover, a novel real-time diagnostic scheme is introduced for fault detection, which operates without additional sensors. This approach effectively distinguishes electrical faults from transient shading effects caused by clouds or soiling, ensuring the system's high efficiency and reliability. Identifying and diagnosing these faults promptly aids in maintaining optimal power output and stability, which is essential for integrating solar energy into the power grid with minimal disruption.

In summary, this thesis not only addresses individual topics within the solar PV sector but also demonstrates how these areas are interconnected, enhancing the overall reliability, sustainability, and cost-efficiency of solar energy generation. Extensive experimental validation underscores the superior performance of these proposed methodologies, affirming their potential in supporting advanced grid integration.

Acknowledgements

It is really challenging to complete this thesis. Without the helpful and supportive persons around me, it is impossible for me to accomplish this task.

First of all. I would like to express my great appreciation to my wife, Yue Cai. Your love and constant support helped me to keep moving forward towards my degree. Thank you for always being there with me, believing in me, and helping me overcome difficulties. Without you, I would spend countless nights worrying about my future and my achievements. I also would like to express my gratitude to my parents and my parents-in-law. Your support and trust really mean a lot to me and give me the power to face challenges.

I would like to express a huge thank you to my supervisor, Associate Professor Weidong Xiao from the University of Sydney. Your support and guidance really helped me a lot in finding the right research direction and getting used to life in Australia. I would also like to express my gratitude to my associate supervisor, Dr. Sinan Li from the University of Sydney.

Furthermore, I would like to express my thanks to Associate Professor Xingshuo Li from Nanjing Normal University. I have learned a lot from you, and your professional advice helped me to solve countless problems during my research. A special thank you also to Professor Yongheng Yang from Zhejiang University. Your guidance and advice make it much easier for me to find the right answer.

I would like to express my great appreciation to the University of Sydney for offering me this opportunity to stay towards a Doctoral degree. Thank you for offering the full scholarship, which really makes the journey much easier.

Finally, I would like to express my great appreciation to all persons I encountered in Australia. Thank you all for making me feel at home.

Thank you all once again from the bottom of my heart.

List of Figures

2.1 The PRC-based PRRC in: (a)P-T domain; (b) P-V domain. 14

2.2 The PV operated in the constant current region. 16

2.3 The experiment's diagram 17

2.4 The solar irradiance profile. 18

2.5 Experimental performance of the APC-based PRRC 19

2.6 Experimental performance of the PRC with fixed ΔV_{pv} 20

2.7 Experimental performance of the PRC with variable ΔV_{pv} 21

2.8 The setting time of the second order under-damped system 22

3.1 How cloud movements affect PV array. 27

3.2 The third degree influence matrix. 27

3.3 Unfolded architecture of the GNN-LSTM model 29

3.4 The spatia-temporal prediction result using the GNN-LSTM model. 31

3.5 Predictive PRRC schemes for (a) Ramp-down control (b) Ramp-up control. 34

3.6 The challenge brought by the prediction error. 35

3.7 The errors conform to Gaussian distribution. 36

3.8 The test system for the predictive PRRC . 38

3.9 Experimental results of the (a)MPPT (b)APC-based PRRC (b)PRC-based PRRC (d) prediction-based PRRC scheme. 39

3.10 Comparison and summary of the experimental results. 40

3.11 Power ramp-down control by predictive PRRC. 41

4.1 Pure data-driven method for Soiled loss estimation. 45

4.2 Perspective mapping from a convex quadrilateral to a rectangle. 46

4.3 Decolorization of PV picture and cell image's division. 47

4.4 A common circuit topology of the PV panel with multiple submodules. 48

4.5 Operation quadrants of PV output. 49

4.6 Confusion matrix comparison (a) pure data-driven model and (b) hybrid scheme. 52
4.7 The error distribution of the estimated soiled loss. 52
4.8 Training progress comparison. 53
5.1 The common faults of PV system. 56
5.2 The electrical performance of CPS fault. 57
5.3 The electrical curves' changes of PV with the intra-line SC fault. 58
5.4 The characteristics of PV with the (a) cross-line fault and (b)line-ground fault. 60
5.5 The fault identification scheme based on PV's long-term characteristics. 62
5.6 The experiment results of the introduced fault detection scheme tested under various scenarios. 63

List of Tables

2.1 Critical parameters of the test system 18

2.2 Comparison of PRRC Performance in the Experiment 18

3.1 Comparison of the Models 33

3.2 Key parameters of the solar PV system 39

3.3 Comparison of the Experimental Results 41

4.1 The Accuracy Comparison of Soiled Loss Estimation 53

5.1 Recorded Experimental Data 63

Contents

Statement of Originality and Scholarship ii

Authorship Attribution Statement iii

Abstract iv

Acknowledgements vi

List of Figures vii

List of Tables ix

Contents x

Chapter 1 Introduction 1

1.1 Background 1

1.2 Motivations and Objectives 3

1.3 Literature Review 5

1.3.1 Solar Power Ramp Rate Control (PRRC) 5

1.3.2 Solar Power Forecasting 7

1.3.3 Solar Photovoltaics (PV) Soiling Loss Estimation 8

1.3.4 Solar PV Fault Diagnosis 9

1.4 Outline 11

Chapter 2 Strategies for PV Power Ramp Rate Control Without Energy Buffer 12

2.1 The Power Ramp Rate Scheme without Extra Energy Storage System 12

2.2 Power Reserve Control with Variable Step Size 13

2.3 Simulation and Experimental Comparison 17

2.4 Power Control Design Considerations 22

2.5 Discussion and Summary 23

Chapter 3 Predictive Approaches to Control PV Power Ramp Rate **25**

3.1 Spatiotemporal Forecasting Model based on Graph Neural Network for Distributed PV system 25

3.1.1 System Model 25

3.1.2 Prediction Results and Evaluations 30

3.2 Predictive Power Ramp Rate Control 33

3.2.1 Control Scheme 33

3.2.2 Challenges of Power-Forecasting-Based PRRC 35

3.2.3 Prediction Confidence with Gaussian Estimation 36

3.2.4 Simulation and Experimental Result 38

3.3 Discussion and Summary 42

Chapter 4 Intelligent Approaches to Estimate Soiling PV Power Losses **44**

4.1 Soiling Loss Estimation based on Deep Neural Networks 44

4.2 Soiling Loss Estimation based on Circuit Topology Analysis and Image Processing 46

4.3 Numerical Validation and Comparison 50

4.4 Discussion and Summary 53

Chapter 5 The Advanced Approaches to Diagnosis Fault in Solar PV Plants **55**

5.1 Faults in the Solar PV Systems 56

5.2 The Complexity of Mismatch Distinguishment in PV Fault Diagnostics 57

5.3 A Novel Real-Time System Identification Approach 58

5.4 Simulations and Experimental Verification 62

5.5 Discussion and Summary 64

Chapter 6 Conclusion **65**

6.1 Overview of Key Contributions 66

6.2 Potential Areas for Future Work 66

Bibliography **68**

CHAPTER 1

Introduction

1.1 Background

As the consequences of human industrial activities become increasingly evident, there is a growing emphasis on transitioning from traditional fossil fuel power generation to renewable energy sources to curb carbon dioxide emissions. Among various renewable sources, solar energy is gaining traction, particularly as the production costs of photovoltaic (PV) panels decline. This trend has prompted increased business investment in the solar power sector, leading to solar energy comprising a larger share of electricity generation. Data from the Australian Renewable Energy Agency (ARENA) from 2015 and 2020 indicates that the cost of large-scale PV power ranged between \$44.50 and \$61.50 per megawatt-hour (MWh). Consequently, the cost of PV power generation is becoming increasingly competitive with that of traditional fossil fuels.

However, the reliability of power generation from PV systems can be inconsistent due to its sensitivity to natural environmental factors, notably solar irradiance and cell temperature. While the cell temperature is typically influenced by environmental temperatures and undergoes gradual changes, solar irradiance can vary dramatically, especially with the transient shading caused by moving clouds. In some extreme instances, the solar power output can plummet to less than 10% of its rated capacity in just a few seconds. This high intermittency and unpredictability in PV power generation pose challenges to its integration into existing power systems.

Rapid fluctuations in solar power generation within PV systems are referred to as solar power ramp events. A power system typically seeks a balance between generation and demand, as imbalances can lead to unstable voltage and frequency levels. In the most severe cases, these power ramp events can cause system collapses, resulting in blackouts. Consequently, monitoring and controlling the power ramp rate of PV systems has emerged as a critical task, especially if there's an intent to incorporate more PV systems into the power grid while ensuring its stability. Many countries have instituted codes and regulations to manage the power ramp rate of solar power generation. Table 1 delineates the power ramp rate limitations across various countries or regions. Conventional approaches employ energy storage systems paired with PV generators to stabilize the power output. However, frequently used storage solutions, such as lithium batteries, are considerably more expensive than PV panels, elevating the total system cost significantly. Furthermore, while PV modules typically have a lifespan of 25-30 years, lithium batteries tend to degrade considerably after a decade, necessitating added maintenance and replacement expenses. Recent studies explore the feasibility of eliminating storage systems altogether, proposing control over the power ramp rate by actively curtailing and reserving a portion of the power generation from the PV units. Nevertheless, this approach grapples with issues like power losses and delayed system responses.

The escalating installation of PV panels introduces additional challenges, particularly in the realms of system maintenance, such as electrical fault diagnosis and soiling detection. Unlike traditional electrical generators that can be rated up to Gigawatts (GW), individual PV panels typically have ratings spanning tens to hundreds of watts. As a result, expansive PV farms can consist of millions of these panels. Even modest residential PV setups designed for rooftop installations may comprise dozens of panels to fulfil local energy needs. Consequently, it is very expensive and labour-intensive to conduct regular checks over the vast number of PV panels. Moreover, the PV panels are usually installed on the rooftops or in rural areas, which makes accessing these panels very challenging and dangerous. Thus, it is difficult to monitor and check their status due to the high cost. Another new challenge is that the data generated by solar systems is much more than that of traditional plants since solar PV panels need to incorporate switching converters to modulate power output. These converters usually consist of multiple sensors to sample electrical signals and micro-controllers to implement maximum power point tracking (MPPT). Hence, efficient data processing methods need to be studied for the improvements of system efficiency and reliability.

With the development of computer science, machine learning-based (ML) approaches have been utilized in a wide range of applications like computer vision, resource allocation, and intelligent network management. The superior performance of ML has been validated in numerous experiments in various areas. Researchers are utilizing ML-based approaches to process the large amount of data obtained from solar PV panels. The strong data analysis ability of ML-based methods can easily extract the complex dependencies and features of the data, which can significantly increase the accuracy of predicting future solar power systems performance. This accurate prediction can lead to precise and efficient power generation control and regulation. Furthermore, the advancement in the image-processing ability of ML-based approaches provides a possible solution for monitoring and maintenance of solar farms. For example, the well-known company DJI has designed and launched a commercial unmanned aerial vehicle (UAV) for solar farm surveillance. This UAV with image processing can monitor solar PV and recognize the hot spots, which shows the possibility of integrating ML-based approaches in regular solar farm maintenance.

However, many challenges still exist in integrating ML-based approaches into solar power generation systems. Incorrect predictions will lead to control mistakes, which can severely harm the system's stability. Therefore, ML-based approaches need to be specially modified to suit the unique needs of solar power generation. As the integration research is still at the early stage, it is necessary to investigate more potential smart schemes for future solar systems with increasing reliability and resilience.

1.2 Motivations and Objectives

This thesis aims to utilize data-driven artificial intelligence (AI) approaches in solving challenges encountered in solar photovoltaics (PV). With the increasing deployment of solar PV panels, more efficient solutions for solar power ramp rate control, soiled loss detection and estimation, and fault detection and diagnosis are required. Additionally, the massive data generated by solar PV systems with real-time processing requirements poses challenges to the storage and computational capability of the current system. To address these challenges, incorporating AI technologies in the solar PV system is considered a feasible solution.

The thesis first investigates the solar power ramp issue. we will review the traditional PRRC schemes that make power generation meet the requirements of regulators around the world. One of the key indicators of these methods is the energy harvest efficiency, as solar panels were relatively expensive in the past. However, more and more research focuses on improving reliability since the cost of PV has increased significantly in recent years. Thus, this thesis aims to thoroughly compare these schemes on the basis of these technical indicators.

Another significant aspect of this thesis is the proposal of a novel DNN-based solar forecasting model for model PRRC schemes that require information on the power generation variation. Since the accuracy of the prediction can significantly affect the control performance, we aim to propose a group solar prediction alogorathim that better focuses the solar vibration based on the cloud movement characters. The model is expected to efficiently extract the graph correlation information of the PV sites and outperform the other DNN-based predictors.

Additionally, the thesis will address the over-regulation issue that is often neglected by PRRC study. This issue will be studied and proven to be a major defect that induces additional power loss. The thesis will also investigate the potential solution to mitigate overregulation by introducing a confidence estimator. This design aims to improve the effectiveness of the PRRC scheme, which can result in higher system efficiency.

Apart from the solar power ramp study, the research will also investigate the common faults in solar systems, which are widely believed to decrease the reliability of PV systems. The work will first study the characteristics of these faults and furthermore propose a new fault identification scheme based on the distinguishment of their long-term electrical performance difference. The methods will not disrupt the normal MPPT operation of the PV system and are independent of extra sensors and equipment.

Finally, the thesis will study the soiling issue of solar PV. Soiling is another common issue that can also decrease the system's efficiency. As the research focuses on large-scale PV farms where regular inspection can be labour-cost, we will introduce a novel soiling estimation method based on advanced image processing techniques and PV circuit modelling. The scheme can be incorporated with UAV to inspect soiling PV for large solar farms with lower lost.

In summary, the objectives of this thesis are to enhance the reliability and resilience of solar PV systems. The thesis studies the advanced solutions to a range of challenges, including solar power vibration forecasting and ramp rate control, electrical fault section and soiling loss estimation. It investigates the feasibility of integrating emerging deep learning into PV systems and develops more efficient, cost-effective, and reliable solutions to those challenges.

1.3 Literature Review

1.3.1 Solar Power Ramp Rate Control (PRRC)

With the higher generation of solar PV to existing power systems, there are growing concerns about the stability of the grid operation [1]. The power generation of solar PV is largely influenced by rapidly changing weather conditions. Thus, the fast variation of solar irradiance can result in significant fluctuations in power ramp rate (RR). This power fluctuation will additionally destabilize the voltage and frequency of the electrical grids [2, 3, 4, 5]. To address this issue, many regions have made specifications and regulations to control the power RR in PV systems [6].

To satisfy these standards, many PPRC methods have been proposed to control the fluctuated generated power [7]. For example, passive approaches will schedule the installation of PV panels in different geographical locations to balance the difference in solar power output[8]. However, these passive approaches are not always effective and can still violate the specifications made by Transmission System Operators (TSOs) [9].

Hence, active PRRC approaches have been proposed to regulate the power generation more efficiently. One of the most common solutions is to install the battery energy storage system

(BESS) to smooth the power output [10, 11]. BESS can serve as an energy buffer that releases power when the solar power generation is low and stores power when it is high[12, 13]. Therefore, BESS can stabilize power output and maintain acceptable RR levels of PV systems [14, 15]. However, BESS usually has a shorter lifespan and higher prices than PV panels, which increases the overall cost of solar power systems [16].

Many cost-efficient alternatives have been proposed. One approach leverages flexible power point tracking (FPPT) to control solar PV power generation directly [17, 18]. Compared with MPPT, FPPT prioritizes power grid stability and allows a certain degree of insufficient power generation [19]. Given the low-cost nature of FPPT [20], it has attracted attention in recent research [21, 22].

Some research focuses on improving existing PRRC approaches. In [23], the authors incorporate active power curtailment (APC) into the conventional P&O MPPT algorithm. This approach enables the PV system to operate normally at the maximum power point and cut power generation when the constraint for RR is violated. However, this method focuses on controlling ramp-up rates and is less efficient in controlling ramp-down rates. Furthermore, this method suffers from problems like measurement delays and algorithmic instability [24]. In [25], the authors proposed to operate PV systems at non-MPPs to eliminate the need for a predictive system and reserve power for RR control. Compared with the approach in [23], [25] can efficiently control both ramp-up and ramp-down rates. However, this approach has the drawback of overregulating power, which may lead to voltage jumps, system instability, and reduced efficiency. Furthermore, the good performance of this method has been only provided in simulation and not in realistic environments that have actual solar irradiance fluctuations[26].

Nowadays, prediction-based PRRC approaches have gained a lot of attention due to the evaluation of data-driven forecasting methods. Under this paradigm, the Photovoltaic (PV) system primarily operates utilizing Maximum Power Point Tracking (MPPT), optimizing solar energy harvesting. The key innovation lies in the system's ability to reduce power generation proactively when a ramp event is anticipated. This predictive approach enables the PV system to adeptly manage ramp rates while simultaneously sustaining high energy generation efficiency.

1.3.2 Solar Power Forecasting

Since the effectiveness of prediction-based PRRC is closely tied to the accuracy of forecasting outcomes, it becomes imperative to conduct a thorough investigation of diverse prediction methodologies and identify the most suitable approach for PRRC. Solar irradiance prediction methods are broadly classified into three categories: physical-model-based, traditional statistical, and machine-learning-based methods.

Physical-model-based approach predicts future solar irradiance by simulating the physical processes of the real world. Given the regular geometrical relationship between Earth and the sun, local non-shading solar irradiance levels can be roughly calculated with knowledge of the global position and the state of PV panel placement [27]. The primary challenge lies in accurately modeling shading effects, especially from cloud movements, which significantly impact PV panel irradiance. Extensive research, including sky image [28], satellite image analysis[29], and ground-based sensor networks [30], has been focused on this aspect, with cloud movement identified as a predominant factor in PV shading.

Traditional statistical method has a long history in solar irradiance prediction, dating back to 1977 with the use of stochastic models [31]. Subsequent studies have explored various time series models such as autoregression (AR), moving average (MA), ARMA, and ARIMA [32, 33], along with Gaussian process models [29] for forecasting solar irradiance and PV power output.

Distinguished from traditional statistical methods, machine learning techniques do not rely on a fixed mathematical model for input data processing and prediction. Instead, they use a training process to develop models specific to the data, even within the same architectural framework. Neural networks (NN) [34, 35] and support vector machines (SVM) [29, 36, 37] are particularly prevalent in solar irradiance prediction. The use of recurrent neural networks (RNN), especially Long Short-Term Memory (LSTM) networks, has been prominent due to their ability to handle sequential data effectively and mitigate issues like exploding or vanishing gradients [38]. Numerous studies have utilized LSTM-based models, often integrated with other predictive methods, for more accurate solar irradiance prediction [28, 39, 40, 41].

Despite the diverse methodologies, most irradiance prediction studies focus on temporal correlations in the time-series data of individual PV panels [42]. However, exploring spatial correlations, especially in areas with densely installed PV panels, offers another rich vein of information yet to be fully mined [43]. In a notable advancement, another study has successfully integrated convolutional graph neural networks (ConvGNN) with Long Short-Term Memory (LSTM) Recurrent Neural Networks (RNN). This innovative approach is specifically tailored to be compatible with photovoltaic (PV) networks. By leveraging the strengths of both ConvGNN and LSTM RNN, this methodology significantly enhances the spatial-temporal prediction accuracy for group solar irradiance [44].

1.3.3 Solar Photovoltaics (PV) Soiling Loss Estimation

Solar photovoltaic (PV) panels have become a crucial source of renewable energy due to numerous advantages, including reduced costs over time [45]. Despite these benefits, challenges like soiling and shading can negatively impact PV efficiency [46]. Soiling— the accumulation of dust and dirt on PV modules— is particularly problematic in large, remote installations where regular cleaning is both difficult and costly [47, 48]. To address this, experts recommend automatic soiling detection to estimate power loss [49].

Traditional research has often used direct measurement approaches to assess power loss from soiling. These methods involve comparing clean and soiled modules or deploying specialized sensors in PV farms [50, 51, 52]. Although effective, these techniques require additional hardware, making them expensive and complex.

Other studies have focused on understanding the material effects of dust, dew, and other environmental factors on soiling [53, 54, 55]. Various mitigation strategies, such as hydrophobic coatings and PV tilt adjustments, have been explored [56, 57]. However, these techniques may be limited by local environmental conditions, making them less universally applicable.

Data-driven models utilizing machine learning and statistical methods offer an alternative approach for estimating soiling loss. These models rely on algorithms and regression analysis to predict future losses or correlate soiling factors [58, 59, 60]. While promising, these methods mainly rely on historical data and may be inadequate for real-time soiling detection.

Innovative solutions have emerged using image analysis techniques for soiling loss estimation. These methods leverage technologies such as deep neural networks (DNNs) to analyze images of soiled PV panels, thereby estimating power loss [61, 62, 63]. DNN-based tools using RGB images also offer the possibility of reducing computational load [64]. However, they generally ignore circuit-level information, potentially limiting their accuracy for high-resolution power loss estimation.

In conclusion, conventional methods for solar PV soiling are costly and only have limited usage under certain environmental conditions. Data-driven methods provide more flexibility but lack the ability for real-time detection. Image processing approaches, especially DRL-based approaches, have both flexibility and real-time detection ability but are currently limited only to image data analysis.

1.3.4 Solar PV Fault Diagnosis

As the installation of PV panels surges around the globe, it is necessary to ensure the system can work in a promising state[65]. Thus, it is crucial to have a reliable fault detection plan for the system. The faults of the PV system can not only degrade the system's efficiency but also induce fire hazards in the case of the work[66]. As a result, the implementation of fault detection is recommended or required by the regulators in many countries [67].

Many fault detection and diagnosis schemes have been proposed in the past years. Methods proposed in [68, 69, 70] are based on PV array output residuals. They involve comparing actual PV outputs with estimated values to distinguish the abnormal state. The estimations rely on additional data such as real-time solar irradiance, temperature, and cloud movements monitored via professional sensors [71]. Consequently, the necessity for extra equipment increases the system's complexity and cost. Some other approaches rely on utilizing time domain reflectometry (TDR) [72, 73]. While these methods leverage the TDR technique effectively, they typically require external equipment to generate specific signals and are predominantly suitable for offline deployment [74].

Moreover, techniques based on the P-V and I-V curves have emerged for identifying faults [75, 76, 77]. hese methods scan the curves and identify faults from the resulting plots. For instance, [75] distinguishes SC faults from shading faults based on the local minimum position on the curves. However, the curve scanning process interrupts the PV system's normal operation, leading to additional power loss, and in some cases, extra circuitry for scanning is required, further escalating costs.

Recent developments have seen fault detection methods utilizing statistics and artificial intelligence. These include algorithms based on artificial neural networks (ANN) [78, 79, 80], support vector machines (SVM) [81, 82], autoregressive models [83], outlier detection [84], k-nearest neighbors [85], fuzzy inference, and multi-resolution signal decomposition [86]. However, these data-driven methods typically rely on data obtained from curve-scanning or additional sensors, inheriting similar flaws as the aforementioned techniques. Additionally, they often require extensive data and computing resources, leading to increased system costs [75].

Driven by the intention to get rid of dependence on additional sensors and curve-scanning, a novel MPPT-based fault detection scheme was proposed in [87]. It will compare the location change of Maximum Power Points (MPP) to identify the electrical fault during operation. The method does not need extra sensors but is less robust to complex scenarios when various errors occur at the same time.

1.4 Outline

This thesis first gives a brief introduction to the rapidly growing solar PV market and then lists the challenges encountered during the growing process. It provides a detailed literature review of previous works and points out the main focus of these works. Specifically, these works focus on increasing the reliability and efficiency of solar power generation.

Chapter 2 elaborates on the DC side of PRRC. It explores the possibility of using BESS-free PRRC approaches in solar PV systems. Specifically, a variable step-size BESS-free PRRC method is proposed. Corresponding simulation results and discussion on power control design constraints are given at the end of this chapter.

Chapter 3 focuses on the prediction-based PRRC method. It first introduces the state-of-the-art graph neural networks (GNN) that can be integrated into distributed PV systems and then evaluates the prediction performance of these data-driven approaches. Specifically, attention is given to the challenges of power-forecasting-based PRRC and the use of Gaussian estimation to enhance prediction confidence. Simulation results and discussions on PRRC design-related constraints are given at the end of this chapter.

In Chapter 4, the thesis shifts its focus to intelligent approaches for estimating soiling losses in PV power systems. This chapter reviews various methods for power loss estimation, including pure data-driven methods and a combination of circuit topology analysis with image processing. Numerical validations and comparisons are presented to illustrate the efficacy of these approaches.

Chapter 5 delves into advanced approaches for diagnosing faults in solar PV plants. It begins with an introduction to various PV faults and the complexities in distinguishing mismatch issues in PV fault diagnostics. The chapter then introduces a novel real-time system identification approach for fault diagnosis, which is validated by experiments.

Chapter 6 elaborates on the contributions of this thesis. Additionally, it provides an overview of possible future works.

CHAPTER 2

Strategies for PV Power Ramp Rate Control Without Energy Buffer

---

This chapter elaborates on an efficient PRRC method that can provide smooth power output without the need for ESS systems. The idea is inspired by the power reserve control(PRC) principles while many improvements are implemented, including various step sizes and smooth power control. The proposed scheme is compared with similar control solutions without ESS integration. The experiment results show more promising control performance with higher ramp rate control success and energy harvest efficiency.

The relevant work has been published in:

- **X. Jiao**, T. Yang, X. Li, S. Ding and W. Xiao, "A DC Side Power Ramp Rate Control Strategy for High Performance and Low Cost PV Systems," in CPSS Transactions on Power Electronics and Applications, vol. 8, no. 2, pp. 128-136, June 2023, doi: 10.24295/CPSSTPEA.2023.00013.

2.1 The Power Ramp Rate Scheme without Extra Energy Storage System

Traditional solutions to eliminate the BESS from PV PRRC can be classified into: passive and active control strategies.

The passive control is implemented by installing the PV systems in a wide range of geographical regions. Thus, the PV panels will not be affected by the clouds' shading at the same time, which results in a smoother power output at the integration point. However, this strategy is less reliable as it is only dependent on the environmental conditions.

On the other hand, the active control is added in the inverter control. It will allow the PV system to operate at sub-optimal conditions to facilitate short-term and appropriate output adjustments. Although this method can lead to less power generation, it provides more flexibility to the power output control. Considering that PV panels are becoming more and more economical, the solution can be implemented in the region where the battery is expensive and solar power ramp rate regulation is strict.

2.2 Power Reserve Control with Variable Step Size

A PRRC scheme based on power reserve can control both ramp-up and ramp-down rates. This scheme is characterized by a power ramp-rate index, as formulated in (2.1). Distinguishing itself from APC, the PRC PRRC scheme adaptively adjusts the time window, denoted as ΔT, and the power differential, ΔP_{pv}. These adaptive adjustments enable a rapid and precise estimation of the PRR, enhancing the control mechanism's efficiency and accuracy.

$$I_{PRR} = \frac{\Delta P_{pv}}{\Delta T} \tag{2.1}$$

The ΔT can be selected as large as several minutes when the local regulator only requires the generator to control the ramp rate at the minute level. However, the measurement windows can be additionally reduced in the PRC-based PRRC so that the operation point never oscillates around MPP. The measurement windows ΔT can be minimized to be only one sampling period T_s to obtain the most prompt PRR detection. Thus, the nearly instant ramp rate can be measured, and the fastest ramp rate control actions can be afterwards taken. The sampling period T_s 's calculation is explained in more detail in the subsection of Power Control Design Considerations' in this chapter.

$$I_{PRR}(T_k) = \frac{P_{pv}(T_k) - P_{pv}\left(T_{k-1}\right)}{T_k - T_{k-1}} \tag{2.2}$$

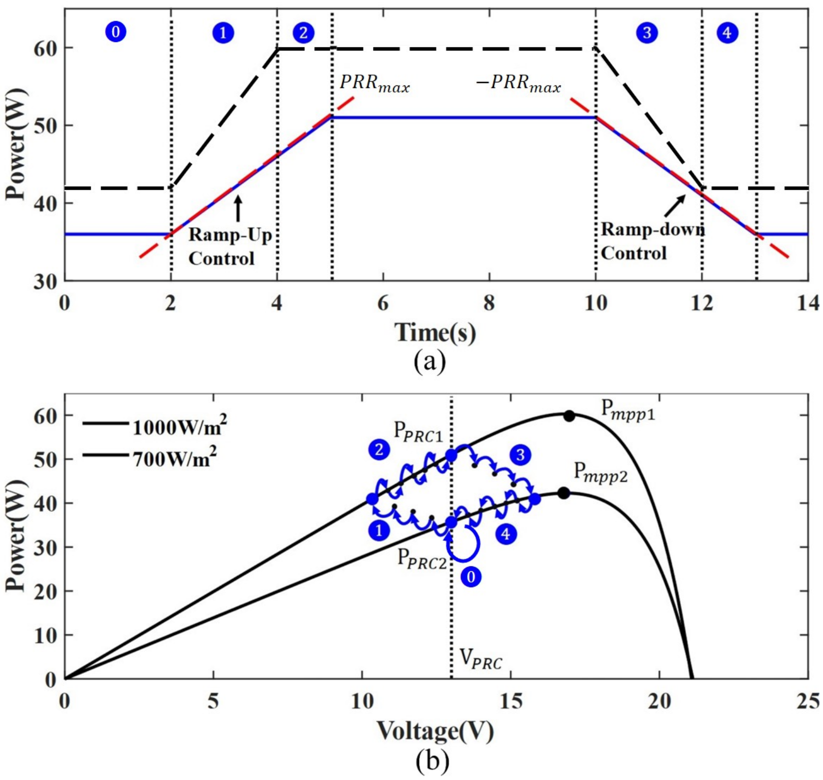

FIGURE 2.1: The PRC-based PRRC in: (a)P-T domain; (b) P-V domain.

The PRC-based PRRC scheme operates by regulating the PV power output at a sub-optimal point, rather than the Maximum Power Point (MPP), to reserve power for ramp-down operations. Fig. 2.1(a) illustrates the operational principle of this scheme, demonstrating how the Power Ramp Rate (PRR) closely follows the guided power-ramp curve to mitigate losses due to mismatches. In this figure, the upper black dashed line represents the actual power variation, while the lower blue solid line indicates the power change regulated by the PRC-based PRRC. In steady-state conditions, the proposed PRRC adjusts the PV voltage to maintain a sub-optimal point for energy reservation, denoted as V_{PRC} in Fig. 2.1(b).

The algorithm of the PRC-based PRRC is predicated on real-time detection ofI_{PRR} as defined by (2.2) and subsequent PV voltage regulation. The voltage reference symbolized as V_{ref}, is updated according to (2.3).

$$V_{ref}(T_k) = \begin{cases} V_{pv}(T_k) + V_{\text{step}}^{\text{curtail}}(T_k), & I_{PRR}(T_k) > 0 \\ V_{pv}(T_k) + V_{\text{step}}^{\text{supply}}(T_k), & I_{PRR}(T_k) < 0 \\ V_{PRC}, & Otherwise \end{cases} \tag{2.3}$$

where $V_{step}^{curtail}(T_k)$ and $V_{step}^{supply}(T_k)$ indicate the adaptive variable step sizes that can drive the PV power rise or fall within the permitted maximal PRR. While the $V_{step}^{curtail}(T_k)$ is applied in the $V_{step}^{supply}(T_k)$ another is used to drive PV supply more power in the ramp-down stage. These two key parameters are are crucial for the operation of the ramp-up and ramp-down stages in the PRRC scheme, respectively. These are expressed in (2.4) and (2.5):

$$V_{\text{step}}^{\text{curtail}}(T_k) = \frac{PRR_{max} \cdot T_s - V_{pv}(T_k) \cdot I_{pv}(T_k) - I_{pv}(T_{k-1})}{2I_{pv}(T_k) - I_{pv}(T_{k-1})} \tag{2.4}$$

$$V_{\text{step}}^{\text{supply}}(T_k) = \frac{-PRR_{max} \cdot T_s - V_{pv}(T_k) \cdot I_{pv}(T_k) - I_{pv}(T_{k-1})}{2I_{pv}(T_k) - I_{pv}(T_{k-1})} \tag{2.5}$$

Their derivation is grounded in the output characteristics of the PV system. Power variation over discrete time intervals is a result of the step changes in voltage and current, ΔV_{pv} and ΔI_{pv}, as described in (2.6):

$$\Delta P_{pv} = V_{pv}(T_k) \cdot \Delta I_{pv} + I_{pv}(T_k) \cdot \Delta V_{pv} + \Delta V_{pv} \cdot \Delta I_{pv} \tag{2.6}$$

Consequently, the step change in PV voltage at discrete time intervals can be calculated using (2.7):

$$\Delta V_{pv} = \frac{\Delta P_{pv} - V_{pv}(T_k) \cdot \Delta I_{pv}}{I_{pv}(T_k) + \Delta I_{pv}} \tag{2.7}$$

where $V_{pv}\,(T_k)\,and\,I_{pv}\,(T_k)$ represent the voltage and current measured at discrete time intervals. A key variable in (2.7) is the change in PV current, ΔI_{pv}.

The PRC-based PRRC scheme operates the PV power at a sub-optimal point situated within the current source region (CSR), as illustrated in Fig. 2.2. Given that the short-circuit current of PV cells is proportionate to solar irradiance, the PV current under the proposed operation is assumed to be proportional to solar irradiance within the CSR. When the sampling

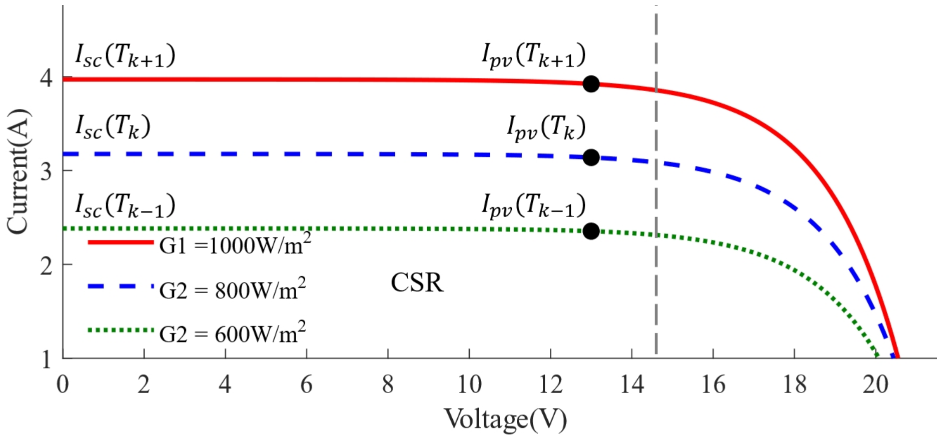

FIGURE 2.2: The PV operated in the constant current region.

rate significantly exceeds the rate of change in solar irradiance, the current variation is approximated in a backward manner, as expressed by:

$$\Delta I_{pv} \approx I_{pv}(T_k) - I_{pv}(T_{k-1}) \tag{2.8}$$

Using (2.7) and (2.8), the step size, ΔV_{pv}, can be determined by (2.9) based on the measured voltage and current at discrete time intervals:

$$\Delta V_{pv} = \frac{\Delta P_{pv} - V_{pv}(T_k) \cdot (I_{pv}(T_k) - I_{pv}(T_{k-1}))}{2I_{pv}(T_k) - I_{pv}(T_{k-1})} \tag{2.9}$$

The magnitude of ΔP_{pv} is set to a predefined parameter representing the upper limit of PRR, denoted as PRR_{max}. The sign of ΔP_{pv} is contingent on the sign of I_{PRR}, dictating the appropriate action for either ramp-up or ramp-down control, as per (2.4) and (2.5).

In summary, the voltage reference is recalculated and updated by the step size $V_{\text{step}}^{\text{curtail}}(T_k)$ upon detecting an increase in power ($I_{PRR}(T_k) > 0$),. This step size, adjustable as per (2.4), is adaptively tuned to the magnitude of power variation. The determination of $V_{\text{step}}^{\text{curtail}}(T_k)$ aims to curtail surplus power, as depicted in stages 1 and 2 in Fig. 2.1. When $I_{PRR}(T_k) < 0$, indicating a power ramp-down stage, the voltage reference is adjusted by the step size $V_{\text{step}}^{\text{supply}}(T_k)$, as outlined in (2.3). The adjustment of this step size is governed by (2.5). The

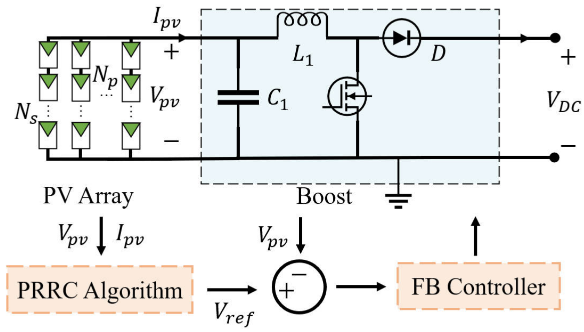

FIGURE 2.3: The experiment's diagram

$V_{\text{step}}^{\text{supply}}(T_k)$ will guide the system to release reserved power to maintain the smoother ramp-down rate. This process is represented in stages 3 and 4 in Fig. 2.1. In situations where $I_{PRR}(T_k) = 0$, the setpoint remains at the predefined level of V_{PRC}, ensuring stability and consistency in the system's operation.

2.3 Simulation and Experimental Comparison

The validation of the proposed PRRC scheme was conducted using a Hardware-In-the-Loop (HIL) platform, demonstrating its effectiveness through comparative analysis with other technologies. As depicted in Fig.2.3, the experimental setup features a typical Photovoltaic (PV) power system configuration. This includes a PV generator coupled with a boost converter. For precise PRRC operation and voltage regulation, the voltage and current of the PV link are monitored at 100 ms intervals. System parameters relevant to the case study are detailed in Table 2.1.

To bolster the experiment's realism, real-world meteorological data, specifically from Melbourne, was utilized. This data, courtesy of the Australian Bureau of Meteorology, is illustrated in Fig.2.4. It showcases significant solar irradiance fluctuations between 9:20 am and 3:40 pm, a period crucial for evaluating the PRRC scheme's performance in terms of energy harvesting and success rate. The experiment sets the power ramp rate's upper limit, PPR_{max}, at ±10 kW/min, aligning with grid codes which mandate that the feed-in power of PV systems should not exceed 10%/min [88].

TABLE 2.1: Critical parameters of the test system

Name	Symbol	Value
Capacity of PV array	P_r	100 kW
Power at MPP	P_{mpp}	305.23 W
Voltage at MPP	V_{mpp}	54.7 V
Current at MPP	I_{mpp}	5.58 A
Open-circuit voltage	V_{oc}	64.2 V
Short-circuit current	I_{sc}	5.96 A
Parallel strings	N_p	66
Series-connected modules	N_s	5
Boost capacitor	C_1	470 μF
Boost Inductor	L_1	5 mH
Switching frequency	f_{sw}	10 kHz
DC-link	V_{DC}	380V

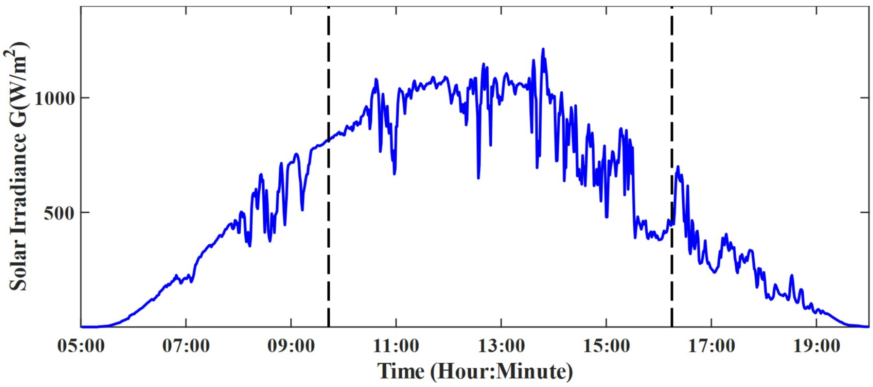

FIGURE 2.4: The solar irradiance profile.

The PRC-based PRRC scheme with variable step size ΔV_{pv} is compared with the method with fixed step size [25] and the APC-based PRRC [23]. The experimental waveforms are recorded and shown in Fig.2.7, Fig.2.6 and Fig.2.5, respectively.

TABLE 2.2: Comparison of PRRC Performance in the Experiment

Cloudy Day			
PRRC scheme	**APC-based PRRC**	**PRC with fixed ΔV_{pv}**	**PRC with variable ΔV_{pv}**
Energy efficiency (η_e)	97.73%	91.23%	92.14%
Success Rate (λ)	26.2%	85.17%	100%
Sunny Day			
PRRC scheme	**APC-based PRRC**	**PRC with fixed ΔV_{pv}**	**PRC with variable ΔV_{pv}**
Energy efficiency (η_e)	100%	92.41%	100%
Success Rate (λ)	-%	-%	-%

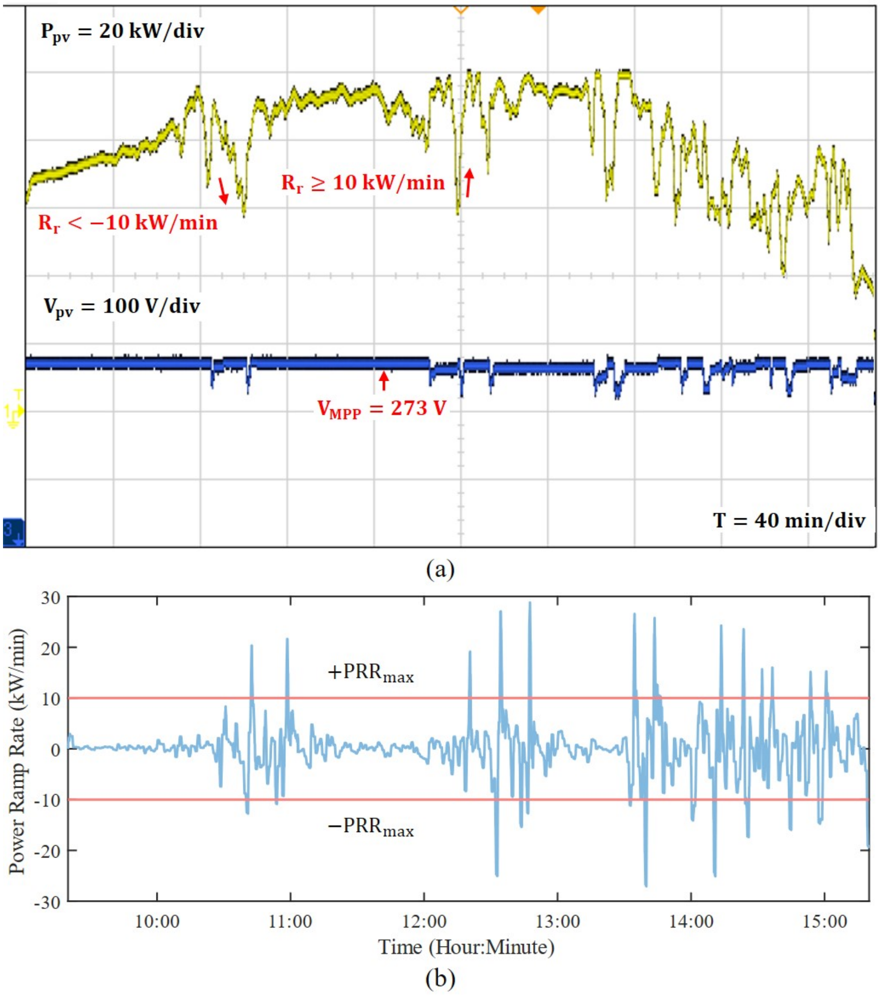

FIGURE 2.5: Experimental performance of the APC-based PRRC

Additionally, Table 2.2 presents a comprehensive quantitative performance comparison of these PRRC methodologies. It reveals that the energy harvest efficiency of APC-based PRRC, at 97.73% (η), is the highest. This high efficiency, however, comes at the expense of diminished control over the ramp-down rate. In contrast, both the PRC-based PRRC with fixed and variable ΔV_{pv}, which operate at non-Maximum Power Point (MPP) points, exhibit lower efficiencies. Nevertheless, the PRC-based PRRC with variable ΔV_{pv}, with an efficiency of 92.14% (η), outperforms the one with fixed ΔV_{pv}, which has an efficiency of 91.23%, attributable to its more balanced regulation actions.

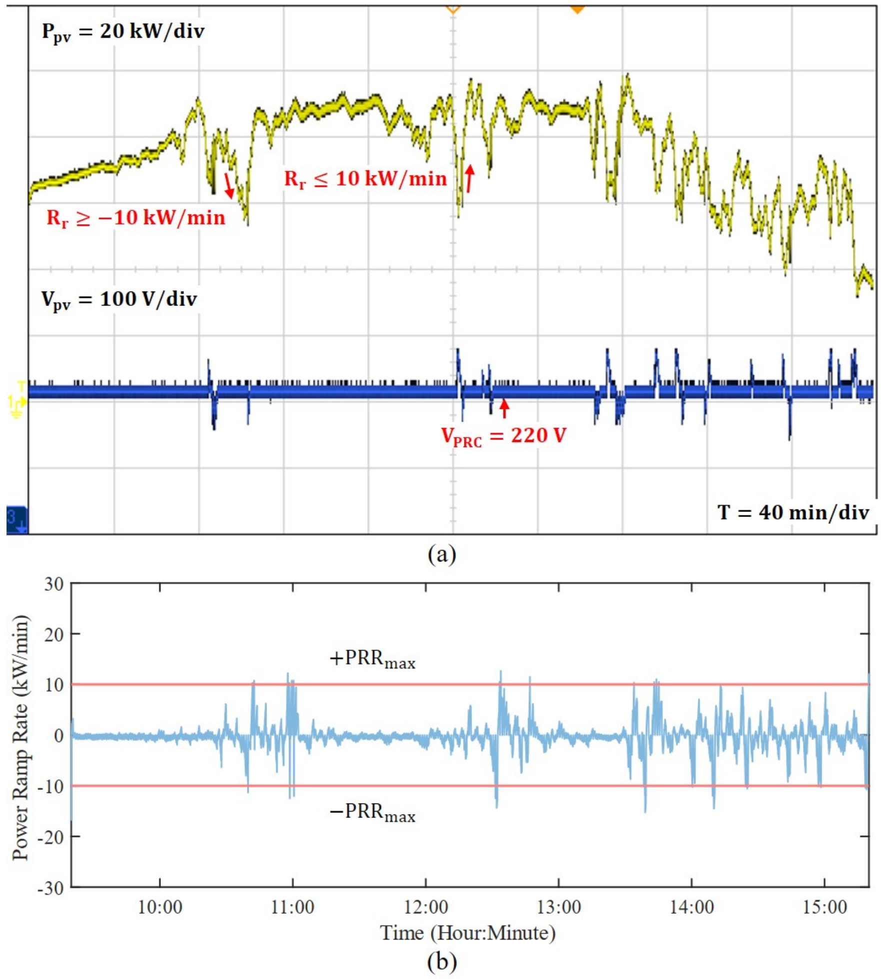

FIGURE 2.6: Experimental performance of the PRC with fixed ΔV_{pv}

In terms of the Power Ramp Rate Control (PRRC) success rate (λ), PRC-based PRRC with fixed and variable ΔV_{pv} display success rates of 100% and 85.17%, respectively. This success rate difference can be partly attributed to their ability to utilize reserved power under continuously decreasing irradiance. Despite these challenges, the variable ΔV_{pv} PRC-based PRRC demonstrates superiority over the one with fixed ΔV_{pv} by more promptly recovering to the target voltage V_{PRC} and being better prepared for future ramp-down control. The APC-based PRRC maintains the lowest PRRC success rate at 26.2% (λ) in the experiment due to lacking ramp-down control.

Table 2.2 also presents the test results for a sunny day for comparison. Since there are no significant power ramp rate events on a sunny day, the success rate is not evaluated. It can be

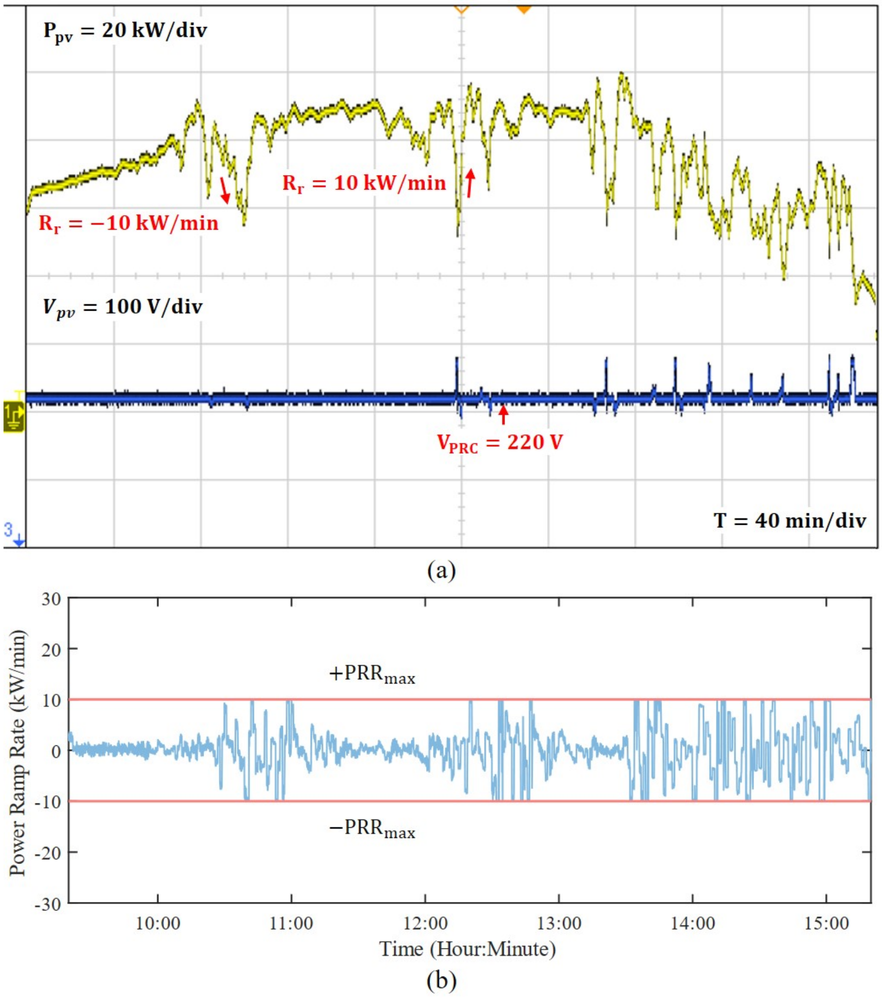

FIGURE 2.7: Experimental performance of the PRC with variable ΔV_{pv}

observed that both the APC-based method and the RC-based PRRC with variable step size achieve 100% efficiency due to zero energy curtailment. However, the PRC-based PRRC with a fixed step size still results in significant deficiencies, as the system always operates in a sub-optimal mode

In summary, the PRC-based Power Ramp Rate Control (PRRC) scheme with variable step size can control both ramp-up and ramp-down rates without the costly BESS. Moreover, it has a relatively higher energy harvesting efficiency with lower failure rates.

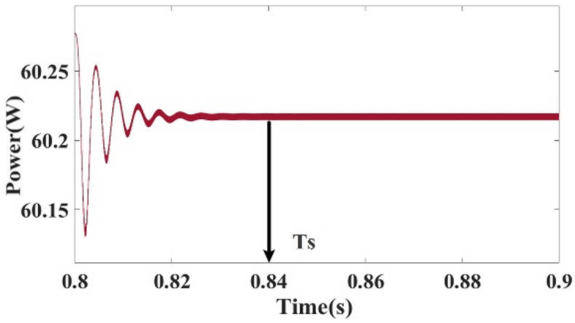

FIGURE 2.8: The setting time of the second order under-damped system

2.4 Power Control Design Considerations

The photovoltaic (PV) panels are commonly connected with switching converters that modulate the operation point of the PV panel and alter its output power profile. However, this power regulation comes with a trade-off: the switching converter, often incorporating energy storage components for voltage and current smoothing, tends to reduce the overall dynamic performance of the system. As a result, damped power oscillations are typically observed during the transient states of each control iteration. If the connected converter functions as an underdamped second-order system, the duration of the transient state power shift is approximately equivalent to the converter's settling time, T_S, as shown in Fig. 2.8.

The sampling time is usually selected to be larger than the setting time to avoid the mismatch at the dynamic period, which can be calculated by

$$T_s \cong -\frac{1}{\xi \cdot \omega_n} \cdot \ln\left(\varepsilon\sqrt{1-\xi^2}\right) \tag{2.10}$$

where $\omega_n = 1/\sqrt{L \cdot C_{in}}$, $\xi = -\sqrt{L}/\left(2R_{pv} \cdot \sqrt{C_{in}}\right)$, and $\varepsilon = 0.1$.

Another pivotal aspect of designing a PRC-based PRRC system involves determining the optimal amount of power to reserve for effective ramp-down control. This decision is complex, as reserving excessive power can lead to significant energy losses, whereas insufficient reservation might result in ramp-down control failures. Unfortunately, there is no universal solution to this dilemma, as the appropriate reserve depends on the specific local irradiance fluctuation conditions. For solar farms experiencing less frequent ramp-down events and only mild reductions in irradiance, it is advisable to reserve a smaller amount of power. This strategy aims to maximize energy harvesting efficiency. Conversely, in locations with rapidly changing irradiance levels, a larger reserve is necessary to ensure the success of PRRC operations. This inherent trade-off in PRC-based PRRC can be mitigated by integrating an irradiance forecasting system. Such a system enables a more predictive approach to PRRC, which will be explored in depth in the subsequent chapter.

2.5 Discussion and Summary

As the share of distributed solar power generation grows within the overall power generation mix in Australia, we need to reconsider traditional practices to handle the variability introduced by resources like PV systems. The key challenges involve adhering to the local grid's operational constraints, focusing on maintaining the electricity supply's quality and avoiding overloads on power lines. Specifically, the power output from individual PV systems can show rapid fluctuations on very short timescales (less than one second) because of quick changes in sunlight levels. These quick changes can disrupt the stability of the electrical network, leading to issues such as voltage flickers. To manage these fluctuations, BESS is usually installed to absorb the fluctuation. Since the BESS can be expensive, it's often also necessary to actively reduce the power output (known as active power curtailment or APC) by controlling the PV inverters and adjusting reactive power to keep the network stable and within operational limits.

This chapter provided an in-depth analysis of a novel PRC-based PRRC strategy for PV systems, operating independently of BESS. This development aligns to maintain the cost-effectiveness of PV power generation. The PRRC scheme, adept at executing both ramp-up and ramp-down operations, demonstrates a significant breakthrough in enhancing energy harvesting efficiency and success rate. The experimental evaluations of this strategy highlighted its superiority, particularly in achieving high energy output and a smooth transition during PRRC operations. This success is attributed to the precise and adaptive sizing of the voltage regulation setpoint, tailored at each time step. The setpoint formulation is based on a detailed examination of PV output characteristics and the dynamic pattern of solar irradiance changes.

While the current chapter focused on evaluating the PRC-based PRRC scheme's effectiveness on a single PV module under singular irradiance vibration conditions, future research could broaden this scope. The next step involves examining the applicability of this scheme to larger PV arrays distributed across extensive geographical areas with diverse solar exposure scenarios. As the power ramp rate can diverge significantly among different installation sites, it is necessary to propose a more delicate control scheme to coordinate all the sub-systems efficiently. Moreover, the current PRC-based PRRC's performance is decided by the selected reservation reference voltage, which relies on the experience and skills of professional people. Future studies should investigate purely data-driven methods that can automatically make decisions based on the local weather conditions and historical system operation data.

CHAPTER 3

Predictive Approaches to Control PV Power Ramp Rate

This chapter presents the integration of the GNN-based spatiotemporal prediction method and the PRRC method. The simulation results validate that this prediction-aided PRRC significantly outperforms conventional PRRC methods. Specifically, prediction-based PRRC achieves higher energy generation efficiency and better ramp rate control results. This is because prediction-based PRRC can foresee the fluctuation of solar irradiance and can adjust power generation accordingly, which results in more efficient energy capture and higher stability of solar PV systems than conventional methods.

Part of the relevant work has been published in:

- **X. Jiao**, X. Li, D. Lin and W. Xiao, "A Graph Neural Network Based Deep Learning Predictor for Spatio-Temporal Group Solar Irradiance Forecasting," in IEEE Transactions on Industrial Informatics, vol. 18, no. 9, pp. 6142-6149, Sept. 2022, doi: 10.1109/TII.2021.3133289.
- **X. Jiao**, X. Li, Z. Ge and W. Xiao, "A Predictive Power Ramp Rate Control Scheme with an Updating Gaussian Prediction Confidence Estimator for PV Systems,"in Solar Energy, vol. 276, pp. 112648, July 2024, doi: 10.1016/j.solener.2024.112648.

3.1 Spatiotemporal Forecasting Model based on Graph Neural Network for Distributed PV system

3.1.1 System Model

Effective utilization of graphical information within a PV network dataset is crucial for exploring its intrinsic spatial dependencies, which then facilitates the formation of an adjacency matrix A. A rudimentary approach might involve connecting nodes to their geographical neighbours. However, this method does not always accurately represent the mutual influence between nodes in a PV network. Consider, for instance, PV1 and PV2 in Fig. 3.1. Their proximity suggests a logical connection, but prevailing wind directions, predominantly vertical in this case, may render their mutual shading influence minimal. Conversely, PV1 and PV3, despite being further apart, might exhibit more similar irradiance variation patterns due to cloud shades passing over both, in line with wind direction. Intriguingly, wind data isn't input as a separate feature but is rather inferred from the group irradiance data.

Another challenge arises from the potential density of the adjacency matrix A. In areas rich in solar resources, PV panels are often installed nearby, leading to a densely populated matrix. This density can impose additional computational demands on the ConvGNN and sometimes even impair the model's performance by introducing misleading information. To address these issues, a targeted approach for defining edges and constructing the adjacency matrix is proposed, focusing on PV groups. This method not only mines graph information more effectively but also enhances the efficiency of the process, ensuring that the spatial correlations within the PV network are accurately and efficiently represented.

$$\mathbf{A} = \begin{cases} a_{i,j} = 1, & R_{i,j} >= \rho \\ a_{i,j} = 0, & Otherwise \end{cases}, \tag{3.1}$$

The mathematical representation of the adjacency matrix $\mathbf{A}$ is crucial in capturing the primary spatial correlation information within the PV network. However, adopting a sparse adjacency matrix $\mathbf{A}$ with a large threshold value ρ can inadvertently result in the omission of some correlation data. This is due to the stringent selection criteria applied in its construction. To mitigate this information loss, the concept of an influence matrix $\mathbf{F}$ is introduced.

$$\mathbf{F} = [\mathbf{A}_1, \mathbf{A}_2, \cdots, \mathbf{A}_K] \tag{3.2}$$

The influence matrix $\mathbf{F}$ is envisioned as an aggregation of multiple adjacency matrices $\mathbf{A}$, each representing varying degrees of spatial correlation based on different threshold values

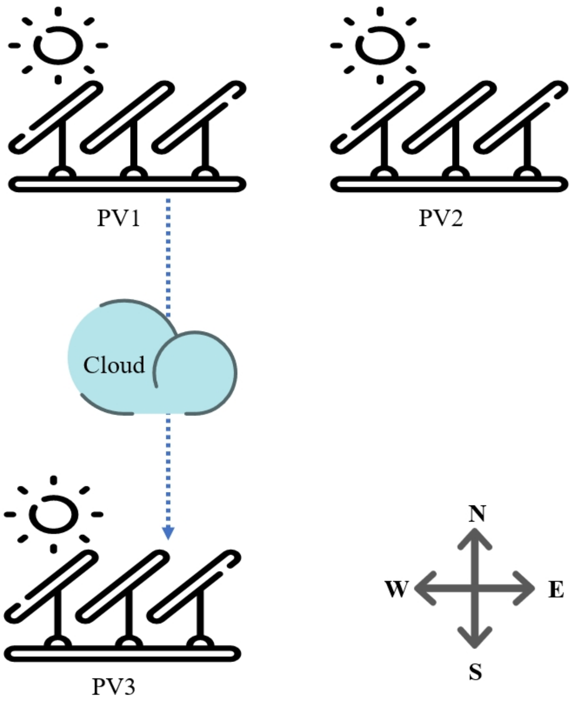

FIGURE 3.1: How cloud movements affect PV array.

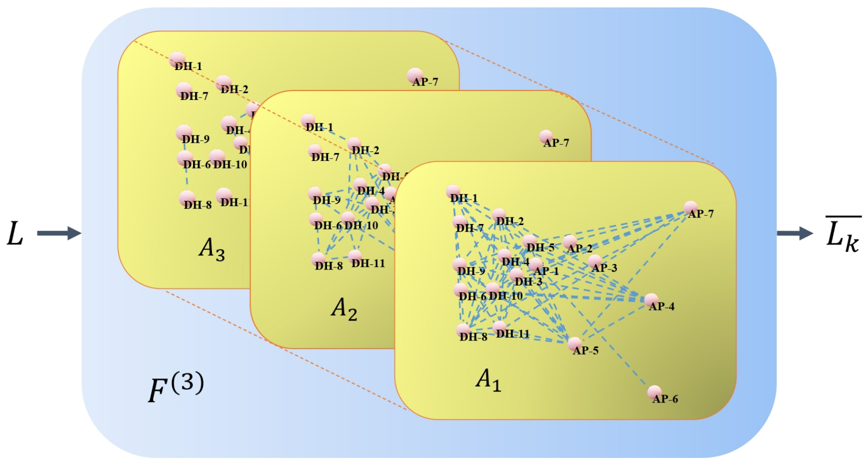

FIGURE 3.2: The third degree influence matrix.

ρ. Formally expressed as $\mathbf{F} \in \mathbb{R}^{M \times M \times K}$, it comprises K adjacency matrices ($\mathbf{A} \in \mathbb{R}^{M \times M}$), arranged in ascending order of their respective threshold values ρ. This construct is defined as a K-degree influence matrix $\mathbf{F}^{(K)}$. The underlying principle in designing $\mathbf{F}$ is to ensure it encompasses sufficient graph information to effectively counterbalance the correlation losses in $\mathbf{A}$. Fig.3.2 illustrates our specifically designed 3-degree influence matrix $\mathbf{F}^{(3)}$.

The normalized graph Laplacian matrix, denoted as $\mathbf{L}$ and belonging to the space $\mathbb{R}^{M\times M}$, is expressed as follows:

$$\mathbf{L} = \mathbf{I}_M - \mathbf{D}^{-\frac{1}{2}}\mathbf{A}\mathbf{D}^{-\frac{1}{2}}, \tag{3.3}$$

To integrate the influence matrix with our graph, a connection between the matrices $\mathbf{L}$ and $\mathbf{F}$ is established through element-wise multiplication. As a larger value of k implies a more comprehensive consideration of correlation in the graph, a k-degree graph Laplacian matrix can be constructed to represent different levels of spatial correlation.

Based on (3.3) and (3.2), the expression for the k-degree graph Laplacian matrix is derived as follows:

$$\overline{\mathbf{L}}_k = \left[\mathbf{L} \odot \mathbf{F}^{(k)}\right]^k \tag{3.4}$$

Here, $\mathbf{L} \in \ R^{M\times M}$ is the normalized graph Laplacian matrix, transformed from $\mathbf{A}$, and $\mathbf{F}^{(k)} \in \mathbb{R}^{M\times M}$ refers to the k-th graph's adjacency matrix as defined in (3.2). $\overline{\mathbf{L}}_k \in \mathbb{R}^{M\times M}$ is the k-degree graph Laplacian matrix, where k-degree denotes the number of correlation graphs in the influence matrix $\mathbf{F}$. Thus, $\overline{\mathbf{L}}_k$ encompasses not only the original graph's information but also additional spatial correlation data. Consequently, the Convolutional Graph Neural Network (ConvGNN) can now be represented as follows:

$$\widehat{\mathbf{x}}_t^{(k)} = f\left(\boldsymbol{\Omega} \odot \overline{\mathbf{L}}_k \mathbf{x}_t\right) \tag{3.5}$$

Here, $\mathbf{x}_t \in \mathbb{R}^{M\times 1}$ is the input data at time instant tt, where $\mathbf{x}_t = \left[\mathrm{ir}_{t,1}, \mathrm{ir}_{t,2}, \cdots, \mathrm{ir}_{t,M}\right]^T$. $\overline{\mathbf{L}}_k$ is the aforementioned k-degree graph Laplacian matrix, and $\boldsymbol{\Omega} \in \mathbb{R}^{M\times M}$ represents the learnable parameters in the ConvGNN. The output $\widehat{\mathbf{x}}_t^{(k)} \in \mathbb{R}^{M\times 1}$ denotes the features extracted by the ConvGNN at time instant t using the k-th degree graph Laplacian matrix $\overline{\mathbf{L}}_k$. To utilize all K levels of spatial correlation information, we denote $\widehat{\mathbf{X}}_t = \left[\widehat{\mathbf{x}}_t^{(1)}, \widehat{\mathbf{x}}_t^{(2)}, \cdots, \widehat{\mathbf{x}}_t^{(K)}\right] \in \mathbb{R}^{M\times K}$ as the collection of output matrices for different values of k at time instance t, which will subsequently be fed into the cascaded LSTM network.

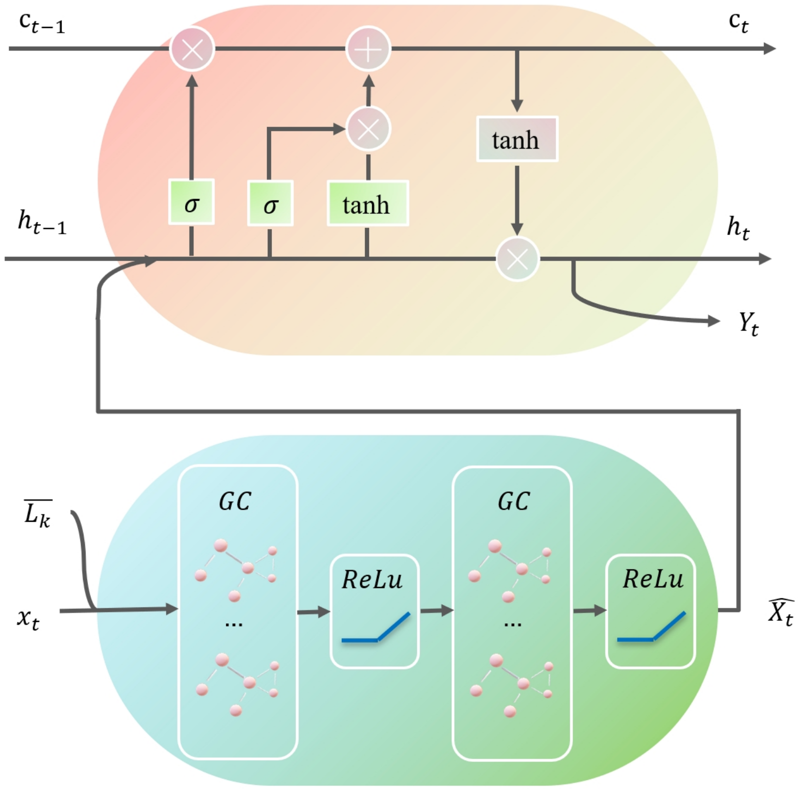

FIGURE 3.3: Unfolded architecture of the GNN-LSTM model

Given the inherent self-correlation within the time-domain data, future datasets can be predicted using historical data via a modified LSTM network, which is composed in conjunction with the previously described ConvGNN (shown in Fig. 3.3).

$$\begin{aligned}
\mathbf{g}_t^{\mathrm{f}} &= f\left(\boldsymbol{\Theta}_f \widehat{\mathbf{x}}_t + \boldsymbol{\Psi}_f \mathbf{h}_{t-1} + \boldsymbol{\epsilon}_f\right) \\
\mathbf{g}_t^{\mathrm{i}} &= f\left(\boldsymbol{\Theta}_i \widehat{\mathbf{x}}_t + \boldsymbol{\Psi}_i \mathbf{h}_{t-1} + \boldsymbol{\epsilon}_i\right) \\
\mathbf{g}_t^{\mathrm{o}} &= f\left(\boldsymbol{\Theta}_o \widehat{\mathbf{x}}_t + \boldsymbol{\Psi}_o \mathbf{h}_{t-1} + \boldsymbol{\epsilon}_o\right) \\
\mathbf{g}_t^{\mathrm{c}} &= f\left(\boldsymbol{\Theta}_c \widehat{\mathbf{x}}_t + \boldsymbol{\Psi}_c \mathbf{h}_{t-1} + \boldsymbol{\epsilon}_c\right)
\end{aligned} \tag{3.6}$$

The symbols $** \in \{forget, input, output, cell\}$ and $\mathbf{g}_t^{**}$ denote the outputs of the corresponding gates at time step t. The function f represents the activation function. $\mathbf{h}_{t-1}$ is the output of the hidden layer from the previous timestamp, and $\widehat{\mathbf{x}}_t \in \mathbb{R}^{KM\times 1}$ is the vector compressed from the input $\widehat{\mathbf{X}}_t$. The learnable parameters for the modified LSTM NN are represented by $\boldsymbol{\Theta}_{**} \in \mathbb{R}^{M \times KM}$, $\boldsymbol{\Psi}_{**} \in \mathbb{R}^{M \times M}$ and $\boldsymbol{\epsilon}_{**} \in \mathbb{R}^{M \times 1}$. The update of the cell state and hidden state is expressed as follows:

$$\begin{aligned} \mathbf{c}_t &= \mathbf{g}_t^{\mathrm{f}} \odot \overline{\mathbf{L}}_K \odot \mathbf{A}_K \odot \mathbf{c}_{t-1} + \mathbf{g}_t^{\mathrm{i}} \odot \mathbf{g}_t^{\mathrm{c}} \\ \mathbf{h}_t &= \mathbf{g}_t^{\mathrm{o}} \odot f(\mathbf{c}_t) \end{aligned} \tag{3.7}$$

It is important to note that the structure of this LSTM differs slightly from the conventional model. The modified LSTM incorporates a weight matrix $\overline{\mathbf{L}}_K \odot \mathbf{A}_K$, which enhances the LSTM NN's ability to consider the influence of neighbouring cell states.

3.1.2 Prediction Results and Evaluations

In this numerical validation, the GNN-based model's performance is evaluated using real-world data and compared against traditional statistical methods as well as other deep-learning-based predictors.

The data for this analysis is sourced from the US National Renewable Energy Laboratory. The dataset comprises readings from 17 silicon radiometers, which are dispersed across Kalaeloa Airport on Oahu Island, Hawaii. Each sensor's location is marked by a white flag, and the names of the sensors are distributed across 17 different locations. The solar irradiance data was collected on July 31, 2010, from 05:50:23 to 19:26:51.

Given that the Global Horizontal Irradiance (GHI) data can range from zero to over a thousand, it is necessary to rescale it. For this purpose, we employ z-score normalization, which transforms the data to have a mean of zero and a standard deviation of one. The z-score normalization process is defined as follows:

$$ir^*_{t,m} = \frac{ir_{t,m} - \mu_m}{\sigma_m} \tag{3.8}$$

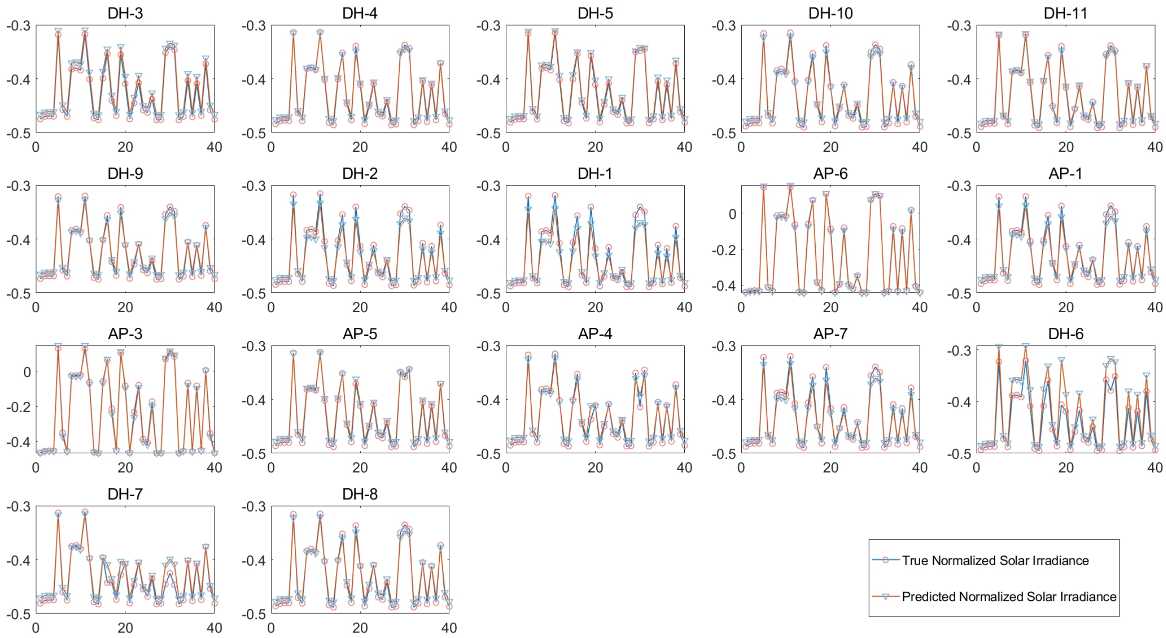

FIGURE 3.4: The spatia-temporal prediction result using the GNN-LSTM model.

In this formula, $ir_{t,m}$ represents any element in the original data IR, μ_m is the mean value of column m in IR, and σ_m is the standard deviation of column m. By substituting all $ir_{t,m}$ values with their normalized counterparts $ir^*_{t,m}$, the data matrix can be converted into its normalized form. The normalized irradiance data typically fluctuates around zero, with positive values indicating performance above average and negative values indicating the opposite.

The predicted results are illustrated in Fig. 3.4 below. It is important to note that the data from all 17 locations were trained together. Evidently, the model adeptly captures the characteristics of irradiance fluctuations, with the predictions closely mirroring the actual values. To mitigate the risks of overfitting and underfitting, the data was shuffled. A testing batch, comprising a 40-second period, was selected to showcase the prediction results. Given that the irradiance data underwent prior normalization, the presented values differ from the original irradiance readings, yet they retain the same vibration trend, which is sufficient for demonstrating the prediction accuracy. If necessary, the original values can be restored through the inverse operation of the z-score normalization process (as defined in (3.8)).

It should also be noted that some locations exhibit superior prediction performance compared to others. This variation can be attributed to the disparity in the amount of information available from the convolutional neural network, as well as differences in the input data across various locations.

The model undergoes further evaluation and comparison against other classic predictive models, including Linear Regression (LR), Moving Average (MA), ARIMA, Support Vector Machine (SVM), and a range of deep network predictors such as conventional Recurrent Neural Network (RNN), Long Short-Term Memory (LSTM), Gated Recurrent Unit (GRN), Attentional LSTM, and CNN+LSTM. The hyperparameters for these benchmark models, such as the number of neurons in each layer and the total number of layers, were optimally tuned or selected based on recommendations from the original literature.

The accuracy of these models is assessed using Mean Absolute Error (MAE), Mean Absolute Percentage Error (MAPE), and Root Mean Squared Error (RMSE), with their respective formulas expressed in (3.9), (3.10), and (3.11).

$$MAE = \frac{1}{N}\sum_{i=1}^{N} |\hat{y}_i - y_i| \tag{3.9}$$

$$MAPE = \frac{1}{N}\sum_{i=1}^{N} \left|\frac{\hat{y}_i - y_i}{\hat{y}_i}\right| \times 100\% \tag{3.10}$$

$$RMSE = \sqrt{\frac{1}{N}\sum_{i=1}^{N} (\hat{y}_i - y_i)^2} \tag{3.11}$$

In these equations, y_i represents the ground truth, $\hat{y}_i$ denotes the prediction results, and N signifies the number of samples.

Table 3.1 presents the prediction results, summarizing the values of MAE, MAPE, and RMSE for comparison. Among them, the two compound models, CNN+LSTM and GNN+LSTM, generally demonstrate superior performance compared to the others. Notably, the proposed GNN+LSTM model achieves the lowest prediction error across all three metrics – MAE, MAPE, and RMSE – thereby outperforming its counterparts.

TABLE 3.1: Comparison of the Models

Model		Evaluation Metrics		
		MAE	MAPE	RMSE
Statistical Models	ARIMA[89]	0.27	26.69	0.35
	LR	0.08	18.11	0.095
	MA	0.076	17.21	0.089
Simple Network	SVM[90]	0.082	18.44	0.097
Deep Networks	GRU[91]	0.027	6.37	0.027
	RNN[92]	0.022	5.35	0.023
	LSTM[93]	0.024	5.13	0.031
	AttentionalLTSM[94]	0.019	4.51	0.022
	CNN+LSTM[95]	0.014	3.61	0.017
	GNN+LSTM	0.0047	1.06	0.0052

Overall, the evaluation substantiates the superiority of GNN+LSTM in terms of accuracy and reliability for solar irradiance forecasting within a distributed PV system context.

3.2 Predictive Power Ramp Rate Control

3.2.1 Control Scheme

The future solar power generation, denoted as $P_{t+\Delta T}$, can be forecasted using the predictor's output Y_t. A potential power drop event is pre-emptively indicated by the predicted ramp rate vibration R_r^{pre}, which is estimated by the following expression:

$$R_r^{\text{pre}} = \frac{Y_t - P_t}{\Delta T} \tag{3.12}$$

where P_t represents the system's current power generation, as directly sensed from the regulation circuit.

Should the predicted future power ramp rate (R_r^{pre} be anticipated to violate grid code regulations (i.e.,($R_r^{pre} < -R_r^{max}$)), the PV output will be proactively reduced to a reference point P_{ref}, as illustrated in Fig. 3.5 (a). This preemptive adjustment aims to curtail the power output in accordance with the grid code limit of $-R_r^{max}$, as expressed in:

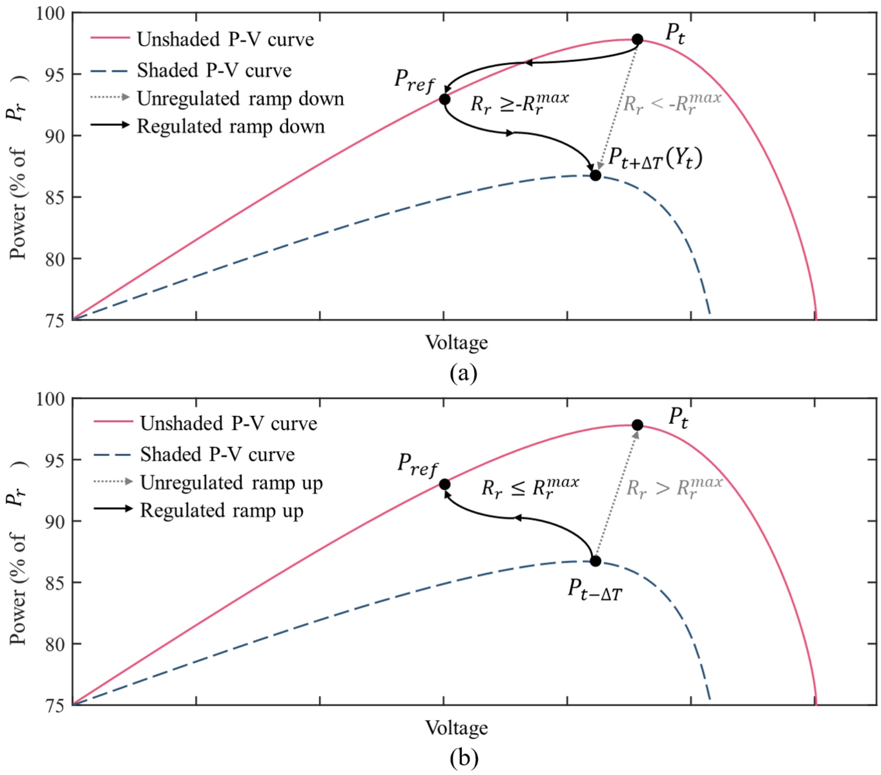

FIGURE 3.5: Predictive PRRC schemes for (a) Ramp-down control (b) Ramp-up control.

$$P_{\text{ref}} = P_t - R_r^{\max} \cdot \Delta T \tag{3.13}$$

$$V_{\text{ref}} \cdot I_t = V_t \cdot I_t - R_r^{\max} \cdot \Delta T \tag{3.14}$$

In this expanded form, I_t and V_t refer to the measured PV operation current and voltage, respectively, whileV_{ref} signifies the reference operation voltage guiding the power regulation. The reference voltage V_{ref} is determined by rewriting (3.14):

$$V_{\text{ref}} = V_t - \frac{R_r^{\max} \cdot \Delta T}{I_t} \text{ if } R_r^{\text{pre}} < -R_r^{\max} \tag{3.15}$$

In a similar vein, the reference operation voltage for ramp-up control is derived as follows:

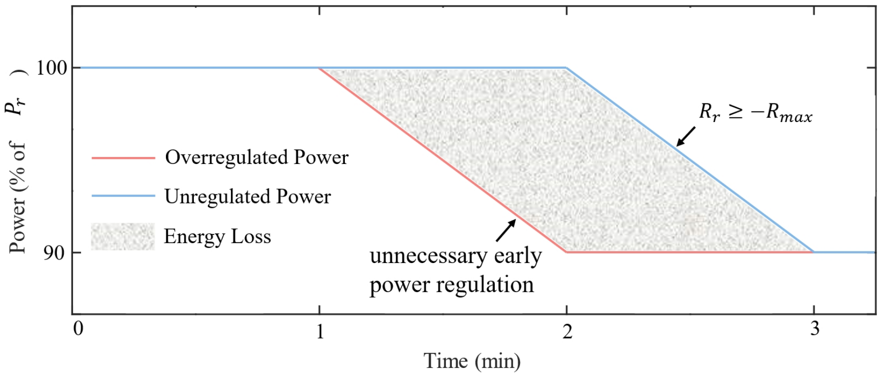

FIGURE 3.6: The challenge brought by the prediction error.

$$V_{\text{ref}} = \frac{V_{t-\Delta T} \cdot I_{t-\Delta T} + R_r^{\max} \cdot \Delta T}{I_t} \text{ if } R_r > R_r^{\max} \tag{3.16}$$

Unlike the prediction-based ramp-down control, ramp-up control does not necessitate additional power reserves and relies solely on historical data and real-time ramp rate measurements. This regulation approach is depicted in Fig. 3.5 (b).

In scenarios where power fluctuations are minimal, the PV system should operate at the Maximum Power Point (MPP) to maximize solar energy harvest. The entire predictive PRRC algorithm proposed here is summarized as:

$$V_{ref} = \begin{cases} V_t - \frac{R_r^{\max} \cdot \Delta T}{I_t} & R_r^{\text{pre}} < -R_r^{\max} \\ \frac{V_{t-\Delta T} \cdot I_{t-\Delta T} + R_r^{\max} \cdot \Delta T}{I_t} & \text{else if} \quad R_r > R_r^{\max} \\ V_{MPP} & \text{otherwise} \end{cases} \tag{3.17}$$

3.2.2 Challenges of Power-Forecasting-Based PRRC

It is crucial to acknowledge that forecasting results can occasionally be inaccurate, potentially leading to overregulation and consequent energy loss. Fig. 3.6 illustrates an instance where power generation could have naturally complied with grid codes but was prematurely reduced due to erroneous forecasting, thus impairing energy harvest efficiency.

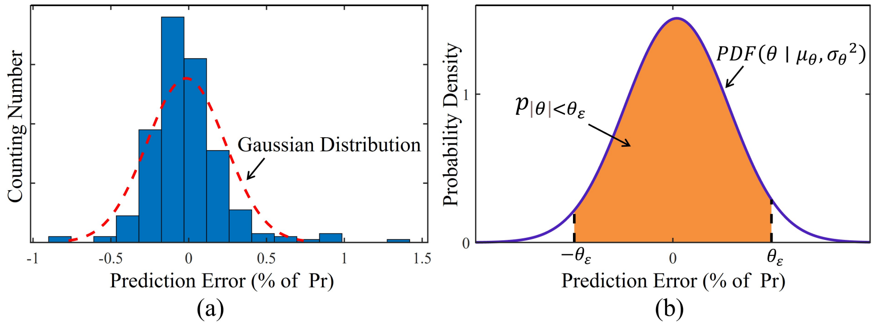

FIGURE 3.7: The errors conform to Gaussian distribution.

The adverse effects of forecasting errors can be alleviated by incorporating a formulated prediction confidence metric into the regulation process, ensuring that advanced regulatory actions are taken only when predictions are deemed sufficiently reliable. The prediction confidence estimator will be introduced in the next subsection.

3.2.3 Prediction Confidence with Gaussian Estimation

Despite endeavors to enhance prediction accuracy, completely eliminating forecasting errors in a prediction-based PRRC system is unattainable. Any prediction error might lead to incorrect actions, potentially resulting in ramp rate control failures. To address this, we propose an estimator that continuously assesses the predictor's recent performance.

This estimator calculates the relative forecasting errors at the last time instant, denoted as $\theta_{t-\Delta T}$, using the currently sampled actual power generation P_t . This calculation is expressed as:

$$\theta_{t-\Delta T} = \frac{Y_{t-\Delta T} - P_t}{P_r} \times 100\% \tag{3.18}$$

Here, $Y_{t-\Delta T}$ signifies the historical prediction result, and P_r refers to the system's rate power.

Fig. 3.7 (a) illustrates the statistical distribution of prediction errors over a specific period $[t - K \cdot \Delta T, t]$where $(K \in N^+)$. For a well-converged prediction model, most errors are observed to cluster around zero, consistent with a Gaussian distribution.

Consequently, the probability distribution function (PDF) for these errors can be derived using equations (3.19), (3.20), and (3.21):

$$\mu_\theta = \frac{\sum_{i=1}^{K} \theta_{t-i\cdot\Delta T}}{K} \tag{3.19}$$

$$\sigma_\theta = \sqrt{\frac{\sum_{i=1}^{K} \left(\theta_{t-i\cdot\Delta T} - \mu_\theta\right)^2}{K}} \tag{3.20}$$

$$PDF\left(\theta \mid \mu_\theta, \sigma_\theta^2\right) = \frac{1}{\sqrt{2\pi\sigma_\theta^2}} e^{-\frac{(\theta-\mu_\theta)^2}{2\sigma_\theta^2}} \tag{3.21}$$

Once the PDF is established, the predictor's recent performance can be quantitatively estimated through the probability interval of the errors, as defined by:

$$p_{|\theta|<\theta_\varepsilon} = \int_{-\theta_\varepsilon}^{\theta\varepsilon} \frac{1}{\sqrt{2\pi\sigma_\theta^2}} e^{-\frac{(\theta-\mu_\theta)^2}{2\sigma_\theta^2}} d\theta \times 100\% \tag{3.22}$$

where θ_ε represents the acceptable boundary for prediction error, and $p_{|\theta|<\theta_\varepsilon}$ describes the predictor's confidence in limiting the error within this range in the recent period.

It is important to note that the integrals in (3.22) cannot be expressed using elementary functions and require assistance from the related error function erf. This equation can be further simplified to:

$$p_{|\theta|<\theta_\varepsilon} = \frac{1}{2}\left[1 + \operatorname{erf}\left(\frac{\theta_\varepsilon - \mu_\theta}{\sigma_\theta\sqrt{2}}\right)\right] \times 100\% \tag{3.23}$$

Finally, the probability $p_{|\theta|<\theta_\varepsilon}$ is compared against a predefined threshold P_φ to assess the prediction's reliability.

The prediction confidence is integrated into the PRRC method to mitigate possible forecasting errors, which is:

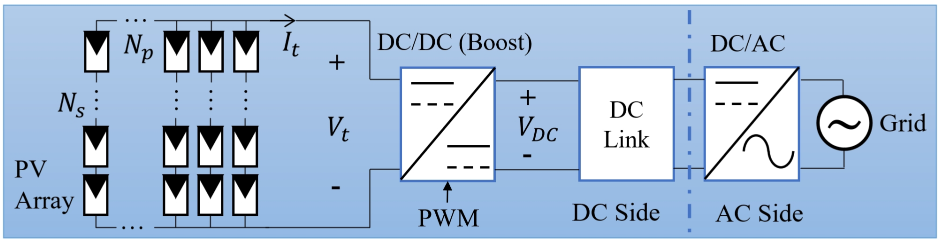

FIGURE 3.8: The test system for the predictive PRRC .

$$V_{ref} = \begin{cases} V_t - \frac{R_r^{\max} \cdot \Delta T}{I_t} & R_r^{\text{pre}} < -R_r^{\max} \cap p_{|\theta|<\theta_\varepsilon} > P_\varphi \\ \frac{V_{t-\Delta T} \cdot I_{t-\Delta T} + R_r^{\max} \cdot \Delta T}{I_t} & \text{else if} \quad R_r > R_r^{\max} \\ V_{MPP} & \text{otherwise} \end{cases} \tag{3.24}$$

In conclusion, this prediction-based PRRC method not only utilizes prediction results but also generates a degree of confidence for these results. By integrating prediction confidence, the algorithm can mitigate the errors in prediction results and can generate more reliable actions.

3.2.4 Simulation and Experimental Result

This section elaborates on the performance of the proposed prediction-based PRRC scheme. Specifically, Fig. 3.8 presents the test system for the proposed approach, a two-stage circuit diagram. It can be seen that the proposed approach is implemented on the DC side to simplify the PRRC process. The key parameters of this test system are summarized in TABLE 3.2.

To evaluate the effectiveness and efficiency of the proposed predictive PRRC scheme, we applied one day's meteorological data (from January 11, 2018) to the test platform. The daily data from Melbourne Airport includes solar irradiance ($\mathrm{W/m^2}$), temperature ($^\circ\mathrm{C}$), wind speed ($\mathrm{km/h}$), relative humidity ($\%$), and cloud amount. The pre-trained Deep Neural Network (DNN) predictor utilizes this data to forecast ramp events for the proposed control algorithm. Additionally, the experiment adheres to the grid codes ($\mathrm{R_r^{max}} = 10\%$) to test PRRC performance. Testing occurred between 9:00 and 12:45, with ramp events concentrated during this period and the process accelerated 30 times to minimize waiting time.

TABLE 3.2: Key parameters of the solar PV system

Name	Symbol	Value
Rated capacity of PV array	P_r	100 kW
Power at MPP	P_{mpp}	305.23 W
Voltage at MPP	V_{mpp}	54.7 V
Current at MPP	I_{mpp}	5.58 A
Open-circuit voltage	V_{oc}	64.2 V
Short-circuit current	I_{sc}	5.96 A
Parallel strings	N_p	66
Series-connected modules	N_s	5
Boost capacitor	C	470 μF
Boost Inductor	L	5 mH
Switching frequency	f_{sw}	10 kHz
DC side voltage	V_{DC}	380V
Proportional factor of PI	P	-0.0317
Integral factor of PI	I	-4.9

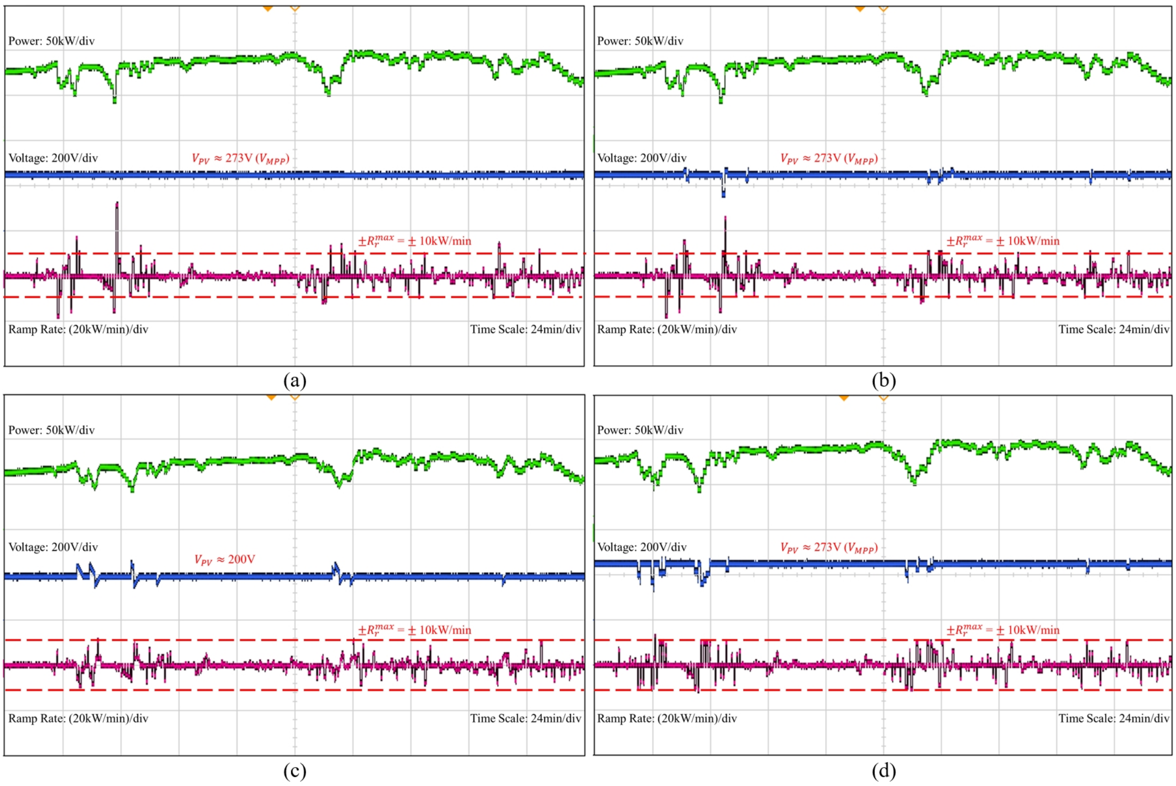

FIGURE 3.9: Experimental results of the (a)MPPT (b)APC-based PRRC (b)PRC-based PRRC (d) prediction-based PRRC scheme.

The proposed predictive PRRC is compared with two classical PRRC schemes without Energy Storage Systems (ESS): APC-based PRRC and PRC-based PRRC. Fig. 3.9 (a) illustrates the

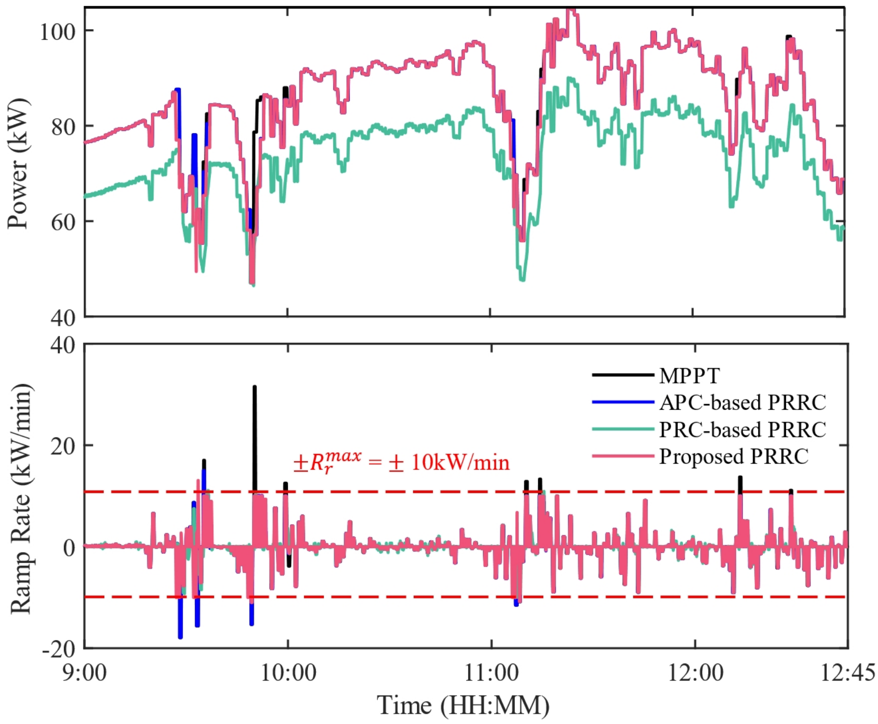

FIGURE 3.10: Comparison and summary of the experimental results.

benchmark condition, where the PV system operates under Maximum Power Point Tracking (MPPT) without ramp rate regulation. This setup results in significant power ramp rates that violate grid restrictions on cloudy days with intense solar irradiance intermittence. Fig. 3.9 (b) presents power changes regulated by the APC-based PRRC, effectively controlling ramp-up events but failing in the ramp-down scenario. Conversely, Fig. 3.9 (c) shows the PRC-based PRRC, which regulates power fluctuations within constraints at the cost of reduced power efficiency, highlighting a tradeoff between ramp rate control success and system efficiency. The proposed PRRC scheme, depicted in Fig. 3.9 (d), operates normally at MPP to optimize power harvesting and actively curtails power only when a ramp-down event is predicted or a ramp-up event is detected, thus effectively controlling power ramp rates while maintaining high efficiency.

For additional evaluation, Fig. 3.10 intuitively compares the regulated power generation and resulting power ramp rates among the four control schemes. The APC-based PRRC and the proposed PRRC show minimal interference with normal power harvesting, unlike the PRC-based PRRC, which significantly reduces power generation. However, the APC-based PRRC

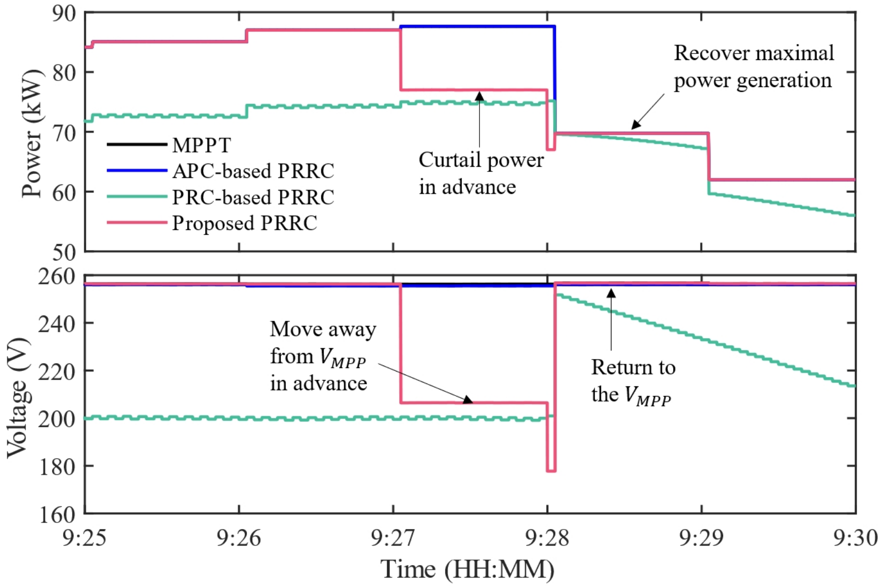

FIGURE 3.11: Power ramp-down control by predictive PRRC.

falls short in controlling ramp-down rates, a gap effectively addressed by the PRC-based PRRC and the proposed PRRC.

TABLE 3.3: Comparison of the Experimental Results

	MPPT	APC PRRC	PRC PRRC	Proposed PRRC
E_{pv} (kWh)	324.99	323.82	277.17	322.98

Table 3.3 summarizes the energy harvest efficiency of the ESS-free PRRC schemes, indicating that the proposed PRRC achieves high energy efficiency (322.98 kWh) while fully controlling the power ramp rate, second only to the MPPT scheme.

Furthermore, Fig. 3.11 offers a detailed view of power ramp-down rate control, highlighting the advantages of the proposed predictive PRRC over MPPT and APC-based PRRC in preventing grid power ramp rate limit violations. The PRC-based method quickly adjusts the PV's power generation in response to power drop events but must then reserve power for potential future events. In contrast, the proposed PRRC can operate at MPP most of the time and reduce the power output when a ramp-down is about to happen.

In conclusion, the proposed method achieves the highest energy generation efficiency compared with other ESS-free PRRC approaches. It can efficiently control ramp-down rates with the aid of the data-driven prediction approach.

3.3 Discussion and Summary

This chapter elaborates on a prediction-based PRRC approach, which marks a significant improvement in the PRRC of solar power systems. Since the performance of predictive PRRC is significantly affected by the accuracy of integrated predictors, the chapter thoroughly studies the main algorithms applied in solar forecasting.

One main aspect of this chapter is to demonstrate a deep learning model used for group solar irradiance forecasting. The model incorporates the CovGNN and LSTM to efficiently mine the key temporal and spatial representations of the PV array's data. The model design considers the intrinsic characteristics of the cloud's movements and influence on PV power generation, which helps it make more accurate irradiance variation results.

Moreover, the chapter proposes a novel PRRC scheme based on the solar foresting results. The chapter also investigates the overregulation problem of PRRC and designs a Gaussian estimator to evaluate the prediction results before making control actions. Therefore, the proposed solution shows an outperforming performance regarding control success and system efficiency.

Another issue acknowledged is the potential inaccuracy of meteorological information obtained from weather stations, which may not be situated adjacent to the PV system. This geographical mismatch in the proposed load forecasting algorithm needs to be addressed. Possible solutions include selecting data from the nearest weather station, employing data preprocessing methods to align nearby weather data with local conditions, or installing basic weather equipment onsite.

Future research can additionally improve the work by incorporating the latest DNN with the attention mechanism. Another path is to combine the predictive PPRC with the existing PV system incorporated with the energy storage system. The combination should aim to reduce the charging cycle of the batter to prolong its lifespan as well as improve the ramp rate control when stored energy is limitted.

CHAPTER 4

Intelligent Approaches to Estimate Soiling PV Power Losses

Chapter 2 and Chapter 3 have demonstrated the solar power ramp event caused by moving clouds' shading and the relevant control strategies to eliminate its negative effects. Besides the deficiency induced by the natural solar irradiance fluctuation, the efficiency of PV plants can also be degraded by other factors like PV soiling or electrical faults. This chapter will investigate PV soiling and introduce a novel power loss estimation method for soiled PV modules. Compared with the solar ramp events that can be controlled with BESS or PRRC schemes, the soiling is induced by the accumulation of dust and thus can not be eliminated from the power control level. The automatic detention and evaluation method can be designed to help the plant operator make regular clean schemes.

The relevant work has been published in:

- **X. Jiao**, X. Li, Y. Yang and W. Xiao. "Novel and Comprehensive Approach for Power Loss Estimation of Soiled Photovoltaic Modules," in Solar Energy, vol. 268, pp. 112283, January 2024, doi: 10.1016/j.solener.2023.112283.

4.1 Soiling Loss Estimation based on Deep Neural Networks

Data-driven models, leveraging machine learning and statistical methods, present an alternative approach for estimating soiling loss on photovoltaic (PV) panels. These methods predominantly utilize historical data to forecast future losses. Recently, innovative solutions have been developed employing image analysis techniques for soiling loss estimation. Specifically, deep neural networks (DNNs) analyze images of soiled PV panels to estimate the associated power loss. This novel method is demonstrated in the current subsection.

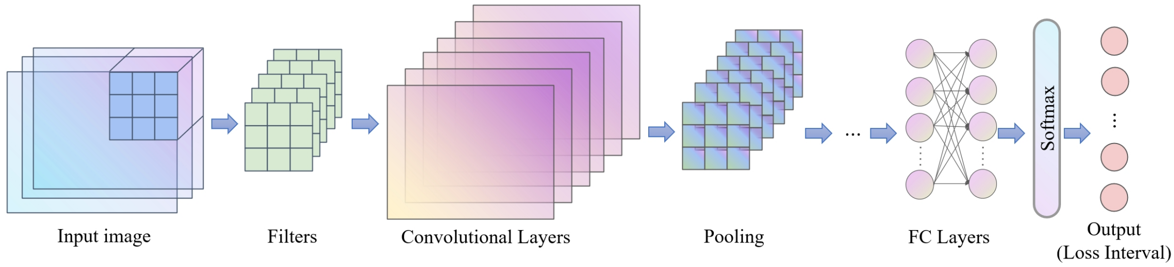

FIGURE 4.1: Pure data-driven method for Soiled loss estimation.

The power loss due to soiling on PV panels was estimated using a DNN-based method. The DNN model is trained with photographs of PV panels. The training labels correspond to measured power loss intervals. Given that the input data comprises images, Convolutional Neural Networks (CNNs) are typically employed to form the core of the DNN model, as illustrated in Fig. 4.1. The CNN architecture is designed to efficiently extract features from the input images via convolutional operations. The deep learning model incorporates down-sampling pooling layers to diminish the matrix size and fully connected (FC) layers for flattening the output. This model processes image data and predicts the estimated power loss for soiled PV panels.

To assess the performance of the proposed method, the DNN-based model is utilized as a benchmark. The structure of the DNN model, detailed in Fig. 4.1, includes an input layer that receives normalized image data. The image undergoes processing through convolution layers, each followed by batch normalization, a ReLU activation function, and a max pooling downsampling layer. The extracted features from these layers are then directed to a fully connected layer for classification.

Throughout the training process, the DNN undergoes multiple epochs, fine-tuning its weights incrementally. With each epoch, the neural network incrementally improves its accuracy in classifying and predicting the categories of the training images. Consequently, as the DNN's performance enhances, the adjustments made to its weights become progressively smaller.

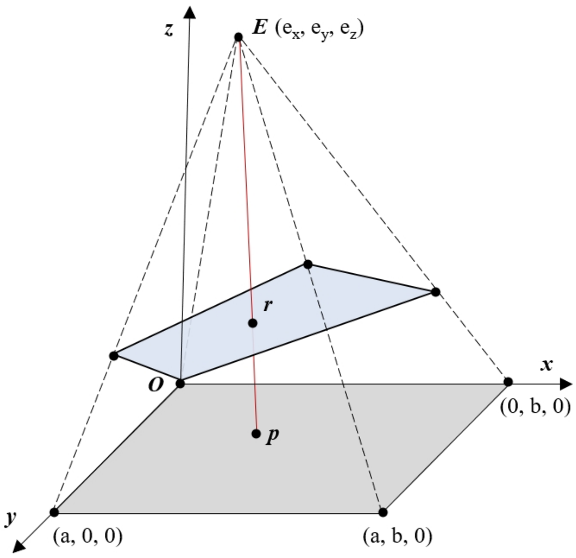

FIGURE 4.2: Perspective mapping from a convex quadrilateral to a rectangle.

4.2 Soiling Loss Estimation based on Circuit Topology Analysis and Image Processing

Previous methods relying solely on image processing techniques tend to overlook the importance of the PV circuit topology, which is rich in information crucial for power generation. As a result, these approaches often yield only satisfactory performance in estimating power losses at low-resolution intervals.

To address this gap, the subsection presents an innovative hybrid model that combines image analysis with circuit topology analysis to estimate power losses in soiled PV modules more effectively. This new approach considers not just the visual data from the panel surfaces, but also incorporates the electrical parameters inherent in the PV circuit layout. The added advantage of this hybrid scheme is that it doesn't require any pre-training, making it well-suited for installations with limited computational resources.

Usually, the solar panels in a raw photo look like irregular four-sided figures. These need to be reshaped into standard rectangular forms. The method used for this is called perspective mapping. The reshaping works by representing each corner of the irregular shape as points $(0, 0, 0)$, $(a, 0, 0)$, $(a, b, 0)$, $(0, b, 0)$ in a 3D coordinate system. For this to happen,

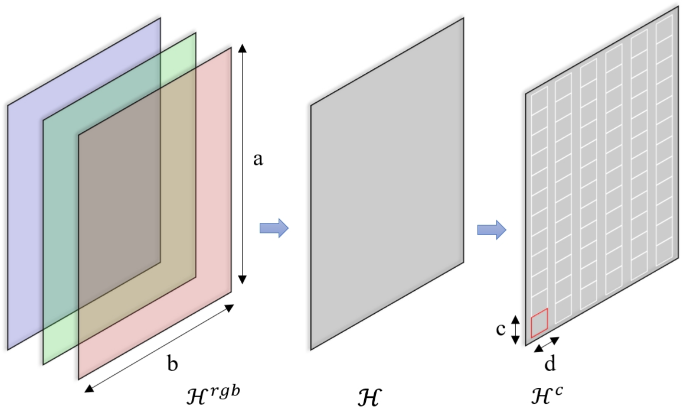

FIGURE 4.3: Decolorization of PV picture and cell image's division.

the viewpoint, given as $E = (e_x, e_y, e_z)(e_z \neq 0)$, needs to be known. A point on the flat plane $p = (p_x, p_y, 0)$ corresponds to a point on the irregular shape $r = (r_x, r_y, r_z)$ as per the viewpoint. This correspondence is explained by the equation:

$$p = E + t \cdot (r - E) \tag{4.1}$$

To successfully perform the reshaping, projections of the irregular shape must be discovered in the flat plane. These projections (p_x in [1,b], p_y in [1,a], and p_z=0) give us the dimensions for the rectangle. Solving this part requires identifying key points like the corners of the shape. Once this is done, the irregular image can be converted into a standard rectangular one. The colour data for this new image is captured in an array:

$$\mathcal{H}^{rgb} = \begin{bmatrix} (p^r_{11}, p^g_{11}, p^b_{11}) & \cdots & (p^r_{1b}, p^g_{1b}, p^b_{1b}) \\ (p^r_{21}, p^g_{21}, p^b_{21}) & \cdots & (p^r_{2b}, p^g_{2b}, p^b_{2b}) \\ \vdots & \cdots & \vdots \\ (p^r_{a1}, p^g_{a1}, p^b_{a1}) & \cdots & (p^r_{ab}, p^g_{ab}, p^b_{ab}) \end{bmatrix} \tag{4.2}$$

To make the processing more efficient, the color in the image is removed, leaving a grayscale picture. This panel image is then broken down into smaller segments (as shown in Fig. 4.3). Each of these smaller images corresponds to the condition of an individual solar cell p^c_{ij}. This

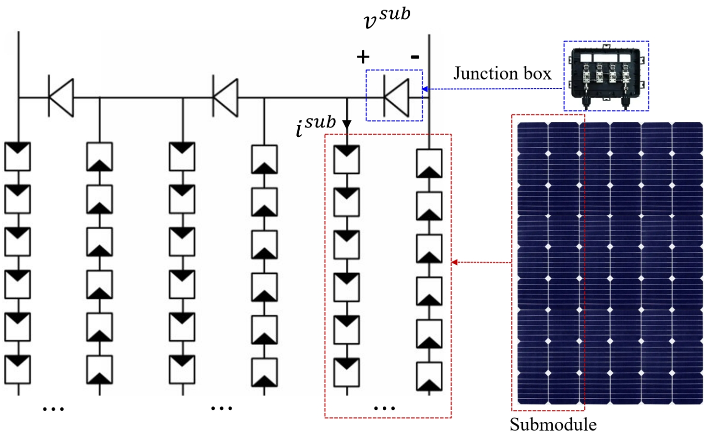

FIGURE 4.4: A common circuit topology of the PV panel with multiple submodules.

average grayscale value for each cell image can be calculated as

$$p^c_{avg} = \frac{\sum_{i=1}^{c} \sum_{j=1}^{d} p^c_{ij}}{c \cdot d} \tag{4.3}$$

Soiled solar cells are flagged when the average grayscale value p^c_{avg} exceeds a certain threshold ε. This threshold is typically estimated from the average grayscale tone of clean solar cells.

To estimate the power loss due to soiling on solar panels, circuit analysis is used. The extent of power loss is closely tied to the panel's internal wiring layout. For the purpose of this study, a standard model as seen in Fig. 4.4 is employed. This model represents a typical solar panel containing multiple smaller units, known as submodules, each made up of a series of individual solar cells. These submodules are generally wired in parallel and feature bypass diodes situated in a junction box. This model serves as a good approximation for most commercially available solar panels.

If it's assumed that each submodule has m identical solar cells, then Kirchhoff's laws for current and voltage provide the following equation:

$$\begin{aligned} i^{sub} &= i^c_1 = i^c_2 = \cdots = i^c_m \\ v^{sub} &= v^c_1 + v^{cl}_2 + \cdots + v^c_m \end{aligned} \tag{4.4}$$

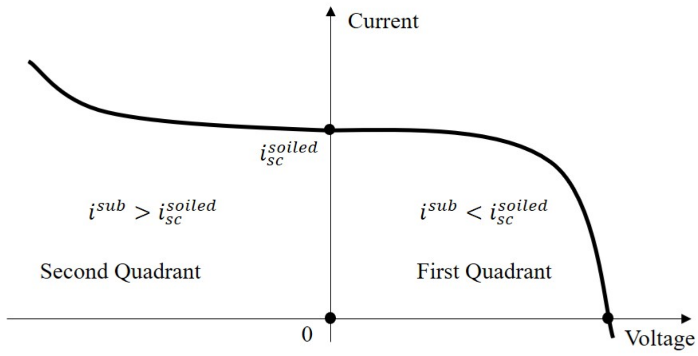

FIGURE 4.5: Operation quadrants of PV output.

In a submodule containing dirty PV cells, the short-circuit current levels follow the relationship $I_{sc}^{soiled} < I_{sc}^{unsoiled}$. As a result, all cells in the submodule can produce power as long as the current i^{sub} remains between 0 and I_{sc}^{soiled}. If i^{sub} goes beyond I_{sc}^{soiled}, the dirty cell shifts to resistive behavior, functioning in the second quadrant as depicted in Fig. 4.5. Because these cells are in a series configuration, this shift impacts all cells, causing them to generate reverse currents. These negative currents, however, are quickly redirected because each submodule is parallelly connected to a diode. Hence, the power output of the submodule is primarily limited by its dirtiest cells, even if most cells are clean. This is commonly referred to as the 'bucket effect,' which can lead to considerable energy losses in dirty PV panels. The power output constraints for a dirty PV submodule and its individual cells are defined as follows:

$$
\begin{aligned}
& 0 \leq i_i^c = i^{\text{sub}} \leq I_{sc}^{\text{soiled}} \\
& v^{\text{sub}}, v_i^c \geq 0, i \in [1, m]
\end{aligned}
\tag{4.5}
$$

The electrical output from the photovoltaic (PV) panel fluctuates in accordance with the shifting count of submodules that are bypassed. Since the PV operation is usually controlled by maximum power point tracking (MPPT) algorithms, the power generation P of a potentially soiled PV panel with n submodules can be derived as

$$
P = \max\{P_0, P_1, \cdots, P_j\} \tag{4.6}
$$

where P_j ($j \in [0, n]$) is the solar power generation when j submodules are soiled and bypassed. In other words, the optimal operating mode can be determined by comparing the power generation across all bypass scenarios. The case is like the partial shading where the P-V curve of the solar system is a multiple-peaks curve. The PV system should operate under conditions that maximize power output while also satisfying the above-derived constraints.

P_j can be calculated by ([96]):

$$\begin{aligned} P_j = & m \cdot (n-j) \cdot v^c \cdot \ldots \\ & \left\{ \log \left[\frac{I_{ph} - i^c - \left(v^c + i^c \cdot R_s\right)/R_{sh}}{I_s} + 1 \right] a \cdot -i^c \cdot R_s \right\} \end{aligned} \tag{4.7}$$

where R_s is series resistance; R_{sh} is the shunt resistance; I_{ph} is the photo current; I_s is the saturation current and a is the modified diode ideality factor.

The maximal power generation of unsoiled PV module is

$$\begin{aligned} P^{us} = & m \cdot n \cdot \left[\left(1 + \frac{R_s}{R_{sh}}\right) a(W-1) - R_s \right] \cdots \\ & \left[I_{ph} \cdot \left(1 - \frac{1}{W}\right) \cdot I_{ph} \cdot \left(1 - \frac{1}{W}\right) - \frac{a \cdot (W-1)}{R_{sh}} \right] \end{aligned} \tag{4.8}$$

where W = Lambert-W$\left\{\frac{I_{ph} e}{I_s}\right\}$.

The power loss P_{loss} ratio is:

$$P_{loss} = \frac{P^{us} - P}{P^{us}} \times 100\% \tag{4.9}$$

4.3 Numerical Validation and Comparison

The data used in this test is from the IBM Research Lab [63]. It includes 45,754 soiled PV photos in wide soiling scenarios. The pure data-driven model is compared as a benchmark to highlight the improvement. The DNN model is trained by 75% of the image datasets and tested by the remaining 25%.

The evaluation of the hybrid scheme involves directly testing all 45,754 PV panel photos, bypassing any pre-training process. This testing aims to determine the accuracy of the scheme in estimating power loss. The error distribution, representing the relative difference between estimated values and labelled data, is displayed in Fig. 4.7. The majority of these errors fall within the range of -5 to 5 percent.

For a comprehensive assessment, the proposed scheme's results are compared with those of a benchmark method based on Deep Neural Network (DNN) classification. This comparison utilizes specific technical indicators to evaluate the accuracy of interval predictions produced by both the proposed scheme and the benchmark method.

$$\text{Recall } = \frac{TP}{TP + FN} \times 100\% \tag{4.10}$$

$$\text{Precision } = \frac{TP}{TP + FP} \times 100\% \tag{4.11}$$

$$\text{Accuracy } = \frac{(TP + TN)}{(TP + TN + FP + FN)} \times 100\% \tag{4.12}$$

where TP denotes the number of true positives, TN denotes true negatives, FP denotes false positives and FN represents false negatives.

Fig. 4.6 displays confusion matrices comparing the proposed method and a DNN model-based method for power loss estimation, with the loss range divided into eight intervals: 0-12.5%, 12.5-25%, and so on up to 87.5-100%. The DNN model, requiring pre-training, is tested with only 25% of the photos. In the matrices, rows indicate predicted classes, and columns represent true classes. Correct classifications are shown on the diagonals, while off-diagonal cells indicate errors. The cell in the bottom right corner reveals each method's overall accuracy. The proposed method achieves a 94.6% accuracy rate, surpassing the benchmark model's 83.6%. Precision rates are listed in the far-right column, and recall rates are in the bottom row. The proposed scheme demonstrates superior precision and recall compared to the DNN model, particularly in distinguishing slightly soiled panels, where the DNN model's precision drops significantly for slots 2-4.

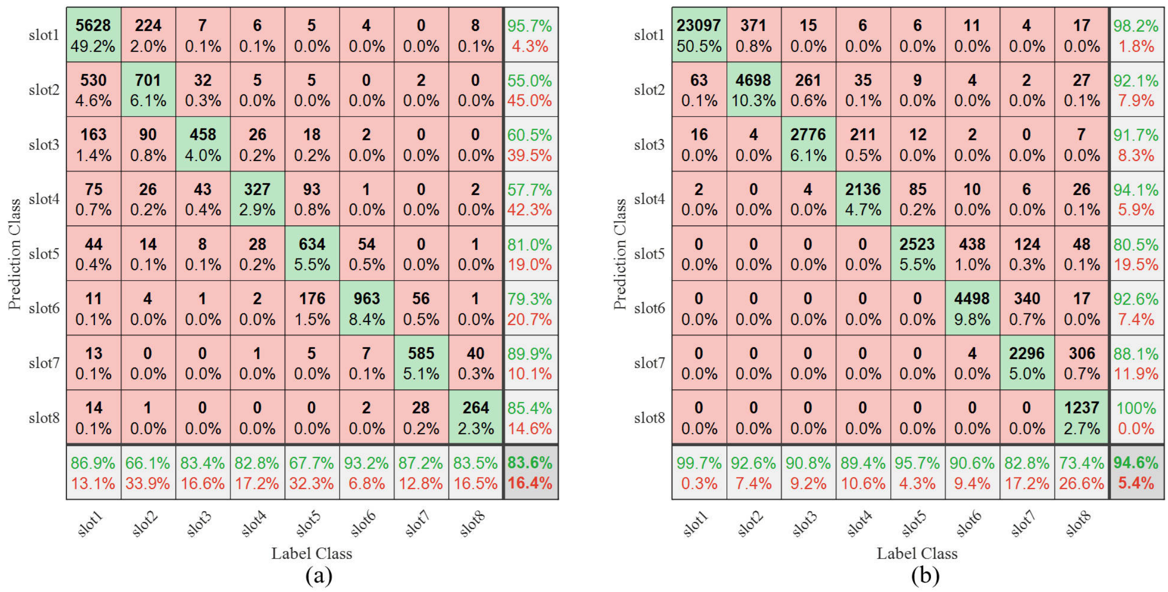

FIGURE 4.6: Confusion matrix comparison (a) pure data-driven model and (b) hybrid scheme.

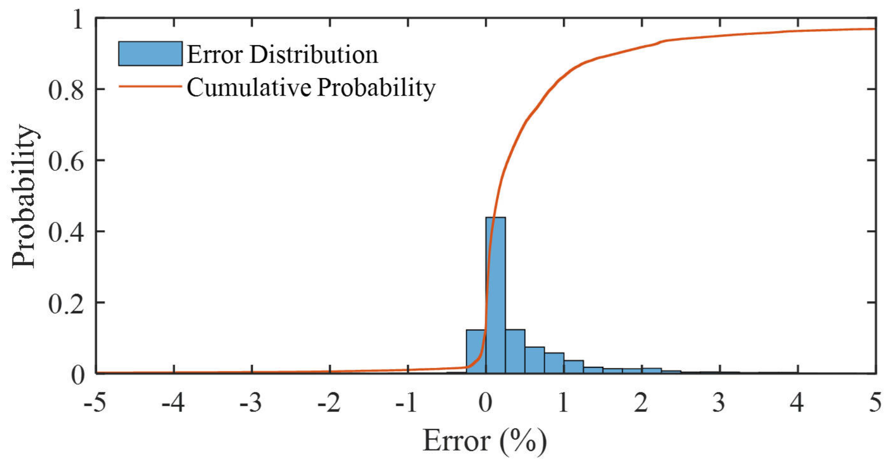

FIGURE 4.7: The error distribution of the estimated soiled loss.

To address scenarios requiring finer power loss resolution, the range was subdivided into 20, 50, and 100 intervals for testing at 5%, 2%, and 1% resolutions, respectively. Due to their large sizes, only the accuracy results of these tests are summarized in TABLE 4.1. The table indicates that while the benchmark DNN model is optimized, it does not perform as well as more advanced models. As resolution increases, the DNN model's accuracy decreases sharply, from 83.58% to 24.61%, whereas the proposed method maintains relatively high accuracy even under stringent resolution requirements.

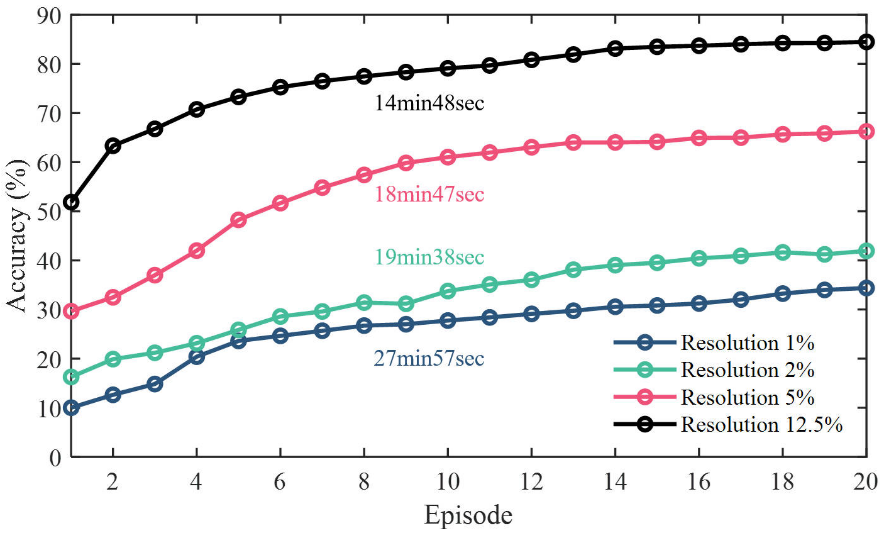

FIGURE 4.8: Training progress comparison.

An additional advantage of the hybrid method is its efficiency, as it eliminates the need for pre-training, unlike traditional DNN-based methods. Fig. 4.8 compares training times for the DNN model across various resolution tasks, highlighting the significant time investment required, which can be even greater for more complex models or larger datasets. In contrast, the proposed method can be applied directly to power loss estimation tasks without incurring these training costs, offering a more practical solution for PV farms with limited computational resources.

TABLE 4.1: The Accuracy Comparison of Soiled Loss Estimation

Resolution	**12.5×8**	**5×20**	**2×50**	**1×100**
Pure data-driven DNN model	83.58%	66.32%	41.97%	24.61%
Hybrid scheme	94.60%	87.61%	75.72%	64.13%

4.4 Discussion and Summary

This chapter discussed the methods to estimate soiled loss for solar PV and introduced a novel hybrid approach for estimating power loss in soiled photovoltaic (PV) panels, combining image processing techniques with circuit topology analysis. The method is tested under diverse soiling conditions and compared with pure data-driven DNN-based estimator.

One of the most significant advantages of the hybrid scheme is its high efficiency, primarily attributed to the elimination of the pre-training process, a standard requirement in conventional data-driven methods. This aspect not only streamlines the implementation but also makes it particularly suitable for PV farms where computing resources may be limited. It has been proved that the proposed method has better performance than the DNN predictor, especially for the scenario with a high prediction resolution requirement. The proposed scheme also shows promising results when the soiling effect is insignificant. In the future, this method can be combined with UAV to monitor large PV farms efficiently.

The limitation of the study is that this method can only be applied to uninformed soiling scenarios. Thus, future research can additionally investigate the uniform soiling by studying the clean PV photo's characters.

CHAPTER 5

The Advanced Approaches to Diagnosis Fault in Solar PV Plants

---

The most critical technical indicator for the PRRC is the solar system's power ramp rates. However, solar power output is influenced by various factors, not just irradiance fluctuations. These include electrical faults, as discussed in this chapter. If such faults occur and are not promptly addressed, the PRRC cannot function as intended. Therefore, developing an effective fault detection method is essential to ensure the system's reliability and the accurate implementation of previously proposed PRRC schemes.

If the electrical fault is not detected and identified, it may significantly decrease the PV system efficiency. In the worst case, it may bring fire risk to the community. Previous detection methods usually require the installation of additional equipment, which increases the overall cost of the system. This chapter will demonstrate a novel fault detection scheme for the PV system. The proposed method does not require additional sensors or other hardware installation. Moreover, the scheme can be combined with the existing MPPT operation of the PV system and will not interrupt its normal operation.

The relevant work has been published in:

- **X. Jiao**, X. Li, T. Yang, Y. Yang and W. Xiao, "A Novel Fault Diagnosis Scheme for PV Plants Based on Real-Time System State Identification," in IEEE Journal of Photovoltaics, vol. 13, no. 4, pp. 571-579, July 2023, doi: 10.1109/JPHOTOV.2023.3262950.

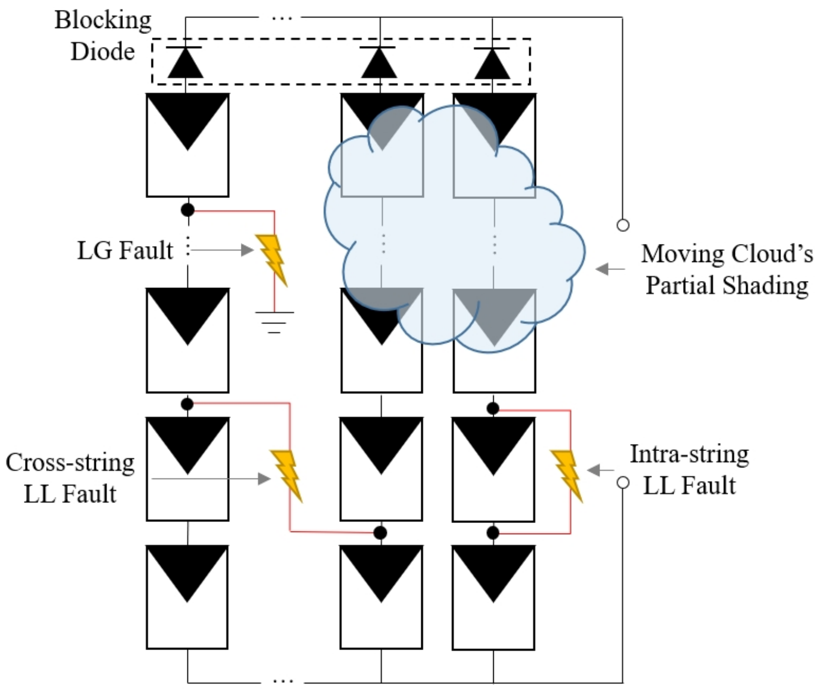

FIGURE 5.1: The common faults of PV system.

5.1 Faults in the Solar PV Systems

The existing faults of the PV system include the open-circuit(OC) fault, short-circuit (SC) fault and the mismatch fault that brought my cloud's partial shading(CPS).

SC faults in PV arrays can be classified into line-to-ground (LG) faults and line-to-line (LL) faults. LL faults are further divided into intra-line faults, where the short-circuit occurs within the same string of PV modules, and cross-line faults, which occur between different strings. This classification is visually represented in Fig. 5.1. There has been some debate in the field, as noted in the literature [97], about the categorization of LG faults, with some experts suggesting that they can be considered a specific type of LL fault due to their similar characteristics.

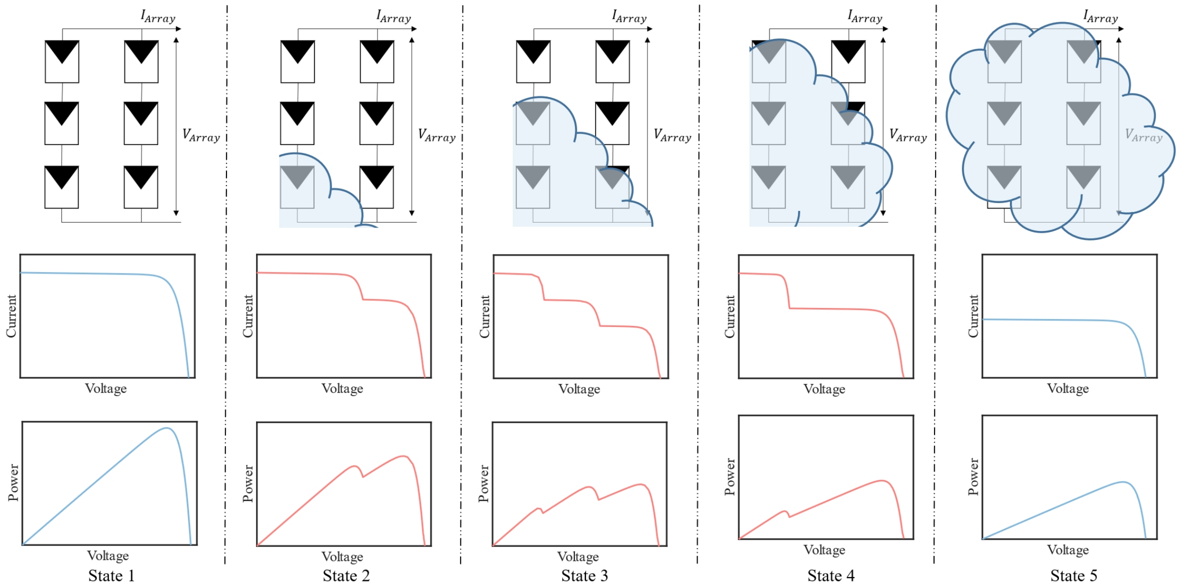

FIGURE 5.2: The electrical performance of CPS fault.

5.2 The Complexity of Mismatch Distinguishment in PV Fault Diagnostics

A primary challenge in the diagnosis of faults is distinguishing the mismatch between Clouds' Partial Shading (CPS) and Short-Circuit (SC) line faults. Both conditions exhibit similar electrical characteristics, making their accurate identification complex.

Fig. 5.2 illustrates the electrical characteristics' changes of a PV array during a CPS mismatch caused by moving clouds. This scenario typically involves a shift from normal operation (State 1) to a malfunctioning state (State 2). Prior research has predominantly focused on analyzing the transient moment when the PV array transitions between these two states. For instance, [75] employs a method of scanning the P-V curve and analyzing the position of the local minimum to identify faults. Similarly, [77] bases its fault detection on the variations in the PV array's open-circuit voltage, short-circuit current, Maximum Power Point (MPP), and other sampled data points. [87] compares the locations and rate of change of the MPPs. However, these approaches rely on contrasting the differences between the transient states, which can lead to inaccurate judgments in scenarios with significant system noise or in complex fault conditions.

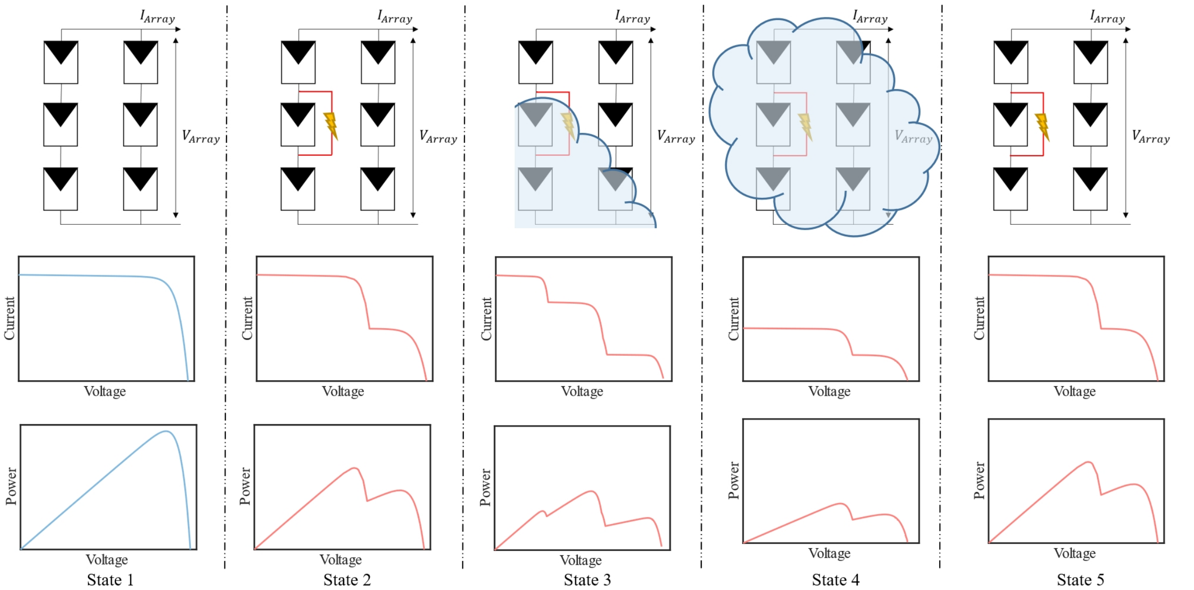

FIGURE 5.3: The electrical curves' changes of PV with the intra-line SC fault.

Moreover, many of these techniques, except [87], require the scanning of the PV array. This process interrupts the system's normal operation, potentially leading to additional power losses and complicating the fault detection procedure. The challenge, therefore, lies in developing a method that can effectively differentiate between SC faults and CPS mismatches without disrupting the PV system's regular functioning. Ideally, such a method should be robust enough to handle complex scenarios and minimize false positives caused by system noise or other external factors. Another design target should be to achieve a balance between reliable fault detection and minimal disruption to the PV system's operation, paving the way for safer and more efficient solar energy production.

5.3 A Novel Real-Time System Identification Approach

To address the above-mentioned challenges, this section introduces a novel real-time system identification approach for fault diagnosis in PV arrays. The scheme can only use voltage and current information sampled during regular MPPT operation to detect emerging faults. This innovative approach allows for potential deployment in almost all existing PV array systems without the need for additional hardware.

The scheme focuses on the long-term characteristics of array faults. Initially, as illustrated in Fig. 5.2, the solar arrays operate without shading, resulting in normal array curves (State 1). From States 2 to 4, clouds pass over the PV array, causing increasing partial shading. This shading is identifiable by the distorted I-V/P-V curves. In State 5, the PV array may become entirely shaded by clouds, leading to uniform solar irradiance and thus, the array curves return to normal. In certain cases where the cloud is small, its shading might pass quickly, also leading to uniform solar exposure. Consequently, it can be inferred that PV arrays naturally recover from partial shading caused by moving clouds, as the clouds eventually pass or uniformly shade the array. This recovery typically occurs within tens of seconds due to the high speed of cloud movement.

On the contrary, the characteristics of Short-Circuit (SC) line faults differ notably from those of Clouds' Partial Shading (CPS) when their long-term behaviours are observed and compared. As depicted in Fig. 5.3, the PV system initially operates under Standard Test Conditions (STC) with an unimodal I-V/P-V curve (State 1). The introduction of an intra-line SC fault leads to distorted I-V/P-V curves indicative of abnormal operation. To simulate challenging scenarios for fault identification, CPS is added in State 3 (partial shading) and State 4 (uniform shading). In State 5, as cloud shading passes, the PV array is exposed to unshaded solar irradiance again. However, unlike the CPS mismatch, the system fails to return to normal operation due to the persistent intra-line SC fault, highlighting a key characteristic distinguishing SC line faults from CPS mismatches.

Furthermore, SC faults can occur in different PV strings or between PV arrays and the ground, as shown in Fig. 5.4. These scenarios are known as cross-line faults and line-ground faults, respectively. Along with intra-line faults, they are collectively classified as SC line faults. The long-term characteristics of these faults concur with the classification criterion: all line faults require manual intervention for resolution. Thus, line faults can be differentiated from CPS-induced abnormalities by examining the long-term characteristics of the PV array.

Before finalizing the fault detection scheme for photovoltaic (PV) arrays, it is crucial to establish the size of the tolerance window, denoted as T_{max}, for abnormal states. The determination of T_{max} is particularly important because the speed of moving shading, which

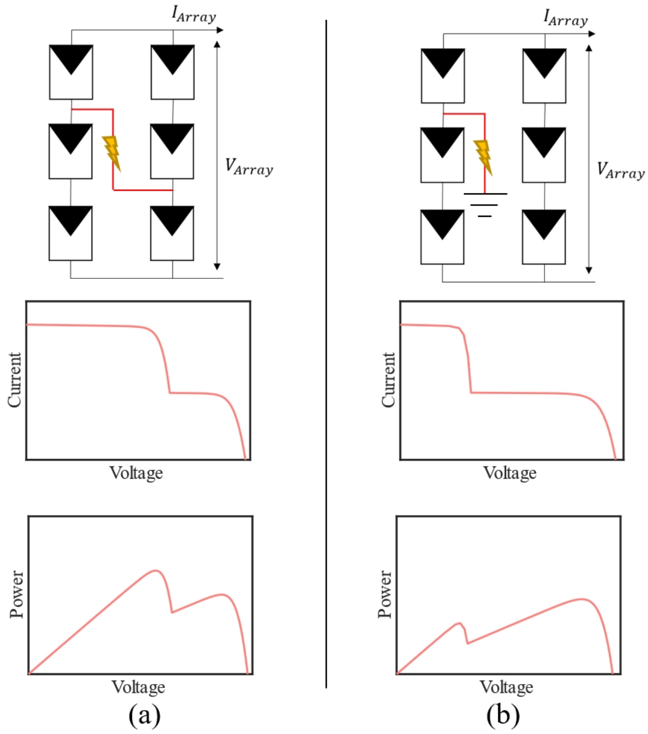

FIGURE 5.4: The characteristics of PV with the (a) cross-line fault and (b)line-ground fault.

generally follows the wind speed, can vary significantly across both temporal and spatial domains. Thus, the local average wind speed,$\bar{V}_{wind}$, is utilized as a key factor in calculating the size of the tolerance window. Thus, the tolerance window can be calculated by:

$$T_{\max} = \frac{D_{\max}}{\bar{V}_{\text{wind}}} \tag{5.1}$$

where D_{max} represents the maximum distance that cloud shading could potentially move across the PV array. Typically,D_{max} is equivalent to the diagonal length of the PV array.

In this scheme, a malfunction is identified as a Short-Circuit (SC) line fault if the duration of the abnormal states,ΔT_{ab}, exceeds T_{max}. The operational condition of the PV array is discerned using the long-term characteristics. If the PV array does not return to normal operation within the time frame of T_{max}, it is reasonable to infer that the system is likely experiencing an SC line fault.

So far, identifying abnormal states in PV arrays still relies on analyzing the P-V/I-V curves, obtained by scanning through all operational states of the system. This process, however, disrupts the normal MPPT operation of the PV systems. To address this issue, the method continues to eliminate the need for curve scanning. Instead, it identifies the array's abnormal states by comparing the estimated and actual MPP parameters.

It's important to note that MPP estimation, which is done by curve-fitting, is accurate only when the PV array is uniformly exposed to solar irradiance. Consequently, the operational condition of the PV array can be determined by constantly comparing the estimated and measured MPP values. Agreement between these values indicates normal operation under uniform solar exposure, while a discrepancy suggests malfunction due to partial shading or a line fault. Hence, the approach does not need to scan the entire I-V or P-V curves.

As both the estimated and actual MPPs can be represented as two-dimensional vectors in the I-V domain, the accuracy of the MPP estimation can be judged based on the relative norm of their difference, denoted as l :

$$l = \sqrt{\frac{\left(V_{MPP}^{est} - V_{MPP}\right)^2 + \left(I_{MPP}^{est} - I_{MPP}\right)^2}{V_{MPP}^2 + I_{MPP}{}^2}} \times 100\% \tag{5.2}$$

where V_{MPP}^{est}, I_{MPP}^{est}, V_{MPP} and I_{MPP} refer to the voltages and currents of the estimated and actually tracked MPPs, respectively.

The state of the PV array is determined by monitoring the value of l. If l is below a small threshold value ϵ, the array is considered to be operating normally. Conversely, a value above this threshold indicates an abnormal state. The scheme can be summarized as:

$$\begin{array}{lr} \text{Normal operation} & l < \epsilon \text{ (always)} \\ \text{Partial shading} & l < \epsilon \rightarrow l \geq \epsilon \rightarrow l < \epsilon \\ \text{Line fault} & l < \epsilon \rightarrow l \geq \epsilon \, (\Delta T_{ab} > T_{\text{max}}) \end{array} \tag{5.3}$$

Fig. 5.5 additionally explains this novel fault identification scheme. It only requires only the PV array's output voltage and current for the judgement. When the PV system operates normally with Global MPP Tracking (GMPPT), the scheme utilizes recent operational data to

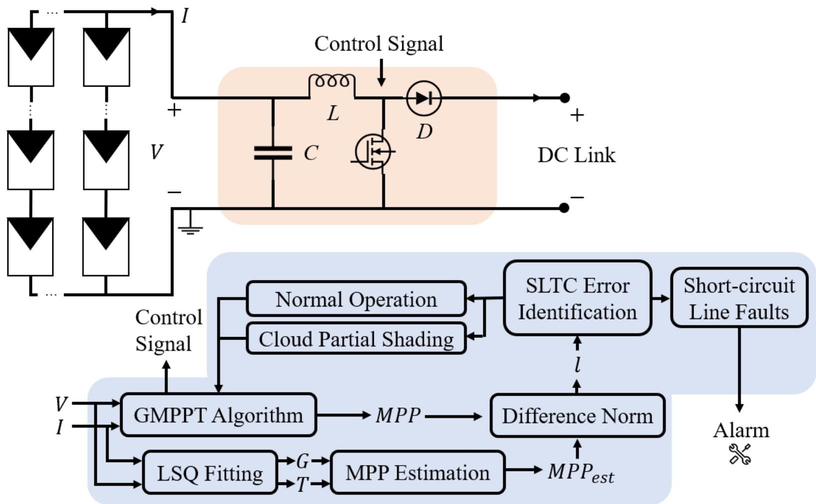

FIGURE 5.5: The fault identification scheme based on PV's long-term characteristics.

assess current solar irradiance and temperature and then compares the current MPP with the actual tracked MPP. The scheme determines the PV array's current state by monitoring the difference norm l and maintains this data for later analysis. Consequently, it can identify the type of fault based on the PV system's long-term characteristics.

5.4 Simulations and Experimental Verification

To validate the effectiveness of the newly developed fault diagnosis scheme for photovoltaic (PV) arrays, comprehensive experiments were conducted. The setup consisted of a 3×2 PV array composed of six SPI-M240W-60IM panels, cascaded by a Boost converter implementing Perturb and Observe (P&O) MPPT.

The experimental results are graphically represented in Fig. 5.6, and the calculated relative difference norms $l(\%)$ are based on currents and voltages sampled during Global MPPT (GMPPT), as summarized in Table III.

Fig. 5.6 (a) shows the PV array under uniform solar irradiance, indicating no SC faults or CPS mismatches. The PV array operates normally, confirmed by consistently low values ($l < \epsilon$), as detailed in Table 5.1.

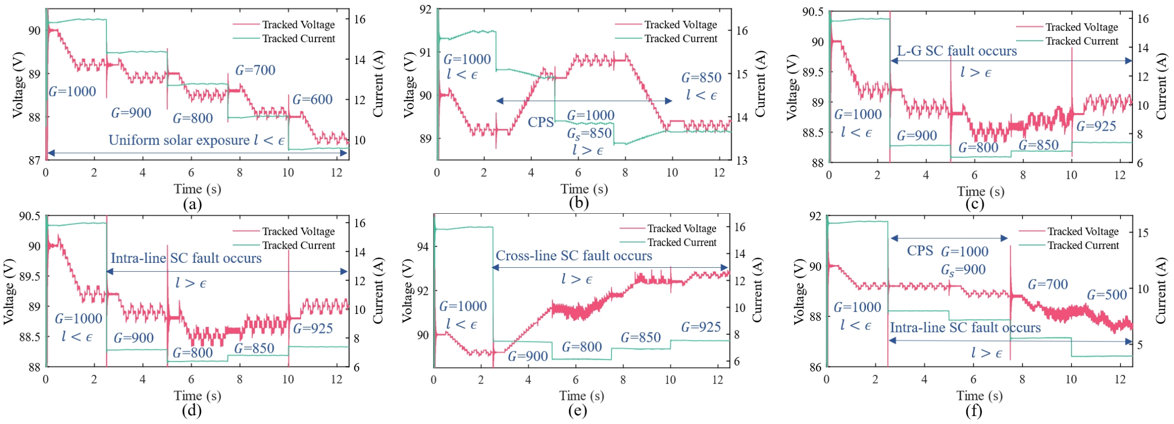

FIGURE 5.6: The experiment results of the introduced fault detection scheme tested under various scenarios.

TABLE 5.1: Recorded Experimental Data

	0-2.5 s	2.5-5 s	5-7.5 s	7.5-10 s	10-12.5 s	Recover ?
Normal	**0.09**	**0.03**	**0.12**	**0.07**	**0.14**	N/A
CPS	**0.10**	1.61	2.00	0.56	**0.22**	Yes
L-G	**0.10**	1.98	3.12	2.50	0.63	No
Intra-line	**0.11**	2.14	2.78	2.74	0.66	No
Cross-line	**0.05**	2.42	2.71	2.47	2.35	No
CPS+SC	**0.11**	12.91	7.50	1.13	2.72	No

Fig. 5.6 (b) shows the CPS mismatch condition. Initially, the entire PV array is unshaded ($G = 1000W/m^2$), resulting in a very low $l = 0.1\% < \epsilon$. Between 2.5 and 10 seconds, partial shading by moving clouds $G = 850W/m^2$ causes a mismatch, reflected by increased l values ($l > \epsilon$). When uniform shading occurs,l drops ($l = 0.22\% < \epsilon$), demonstrating the system's recovery from CPS mismatch, as identified by the scheme.

Fig. 5.6 (c), (d), (e)) show different types of SC faults (intra-line, cross-line, and line-to-ground) are simulated. In each case, l consistently exceeds the threshold ϵ and does not revert, indicating persistent faults. The scheme effectively identifies these abnormalities, differentiating SC faults from CPS mismatches, and signals the need for manual intervention to prevent potential hazards.

Fig. 5.6 (f)) shows the concurrent CPS mismatch and SC fault. This extreme scenario showcases the robustness of the method. Initially, the system operates normally ($l = 0.11\% < \epsilon$). Upon simultaneous application of CPS mismatch and SC fault at 2.5 seconds, l surges

($l = 12.91\% > \epsilon$). After the CPS mismatch ends at 7.5 seconds, l remains high due to the SC fault, validating the scheme's ability to detect SC faults amidst complex conditions.

In conclusion, the experimental outcomes affirm that the introduced scheme can effectively differentiate between normal operation, CPS mismatch, and SC faults in PV arrays by monitoring the relative difference norm l. Its ability to identify SC faults, even in challenging scenarios, underscores its robustness and potential for enhancing PV system safety.

5.5 Discussion and Summary

This chapter introduced a novel fault diagnosis scheme for the solar PV system. This scheme adeptly differentiates SC line faults from the effects of MCPS, a common challenge in the operation of PV systems.

A critical advancement of the introduced scheme over traditional methods is its elimination of the need for additional sensors, equipment, or the system's disconnection for curve-scanning. These conventional approaches often incur extra costs and cause operational interruptions. The proposed fault detection scheme can be combined with PV MPPT, which will not interrupt its normal operation.

Moreover, the method is based on the long-term charter of PV system, which makes it robust to the short-term noise. The above simulation and experiments have proved that the proposed scheme can detect the fault accurately and efficiently in a wide range of testing scenarios.

This work only analysis the data sampled in the steady state. Future work can additionally investigate the possibility of detecting the faults while the PV system is working in the MPPT transient state.

CHAPTER 6

Conclusion

In conclusion, this thesis has extensively explored various challenges and potential solutions within the solar photovoltaics (PV) industry.

Chapter 1 introduces the thesis background, research motivations, and a review of recent studies.

Chapter 2 discusses the DC side of PRRC, focusing on BESS-free methods in solar PV systems and detailing a variable step-size approach. Simulation results and design constraints for power control are summarized.

Chapter 3 examines prediction-based PRRC, highlighting the integration of state-of-the-art graph neural networks (GNN) into PV systems and evaluating their performance. The chapter concludes with simulation results and discussions on PRRC design constraints.

Chapter 4 addresses intelligent methods for estimating soiling losses in PV systems, reviewing both data-driven methods and combinations of circuit analysis with image processing. Efficacy is shown through numerical validations and comparisons.

Chapter 5 covers advanced diagnostic approaches for PV faults, introducing a novel real-time identification method and discussing its validation through experiments.

This chapter summarizes the thesis and outlines the main contritions and future works.

6.1 Overview of Key Contributions

The main contributions are summarized as:

- The thesis has reviewed the solar power ramp rate control scheme and demonstrates the two novel ESS-free PRRC schemes proposed by the author.
- The thesis has made a comprehensive review of the existing solar prediction models and demonstrates one graph neural network-based predictor proposed by the author.
- The work has discussed the common electrical faults of solar PV systems and analysed the main challenges to detect and distinguish these faults. Additionally, a novel fault detection method proposed by the author is demonstrated.
- The thesis analysed the soiling issue of PV systems and reviewed the recent deep-learning-based solutions. A hybrid method based on PV image analysis and PV modelling is then introduced.
- The thesis summarized the main challenges brought by increasing solar power capacity and investigate the intelligent solutions to improve PV system reliability and resislience.

6.2 Potential Areas for Future Work

Future research should continue to refine these methodologies, focusing on real-world application and scalability. It is also imperative to explore the integration of emerging technologies, such as artificial intelligence and IoT, with traditional energy systems to create a more adaptive and resilient energy infrastructure.

For the power ramp rate control, future studies can investigate the possibility of grouping PV panels with various solar exposure conditions. In such diverse settings, power ramp rates can differ greatly among individual PV modules. Addressing this variability necessitates the formulation of sophisticated strategies for synchronized module operation, thereby improving the aggregate efficiency and adaptability of the entire system.

Moreover, there is considerable scope for investigating advanced deep-learning models and integrating more refined forecasting techniques. These developments could significantly advance PRRC's capabilities in the dynamic field of solar energy. Current DNN prediction models require substantial computational resources. Hence, there is a pressing need for more accurate yet less complex prediction algorithms. Such innovations would not only enhance prediction accuracy but also reduce the computational burden, making these models more accessible and practical for widespread application.

With the growing deployment of PV panels, developing robust methods for detecting malfunctions like electrical faults, partial shading, and panel soiling becomes increasingly crucial. Effective fault detection is imperative for maintaining system efficiency, ensuring normal operation, and mitigating potential hazards. Future research should focus on creating more effective diagnostic tools and methodologies to identify and address these issues promptly and accurately.

Bibliography

[1] Tomonori Sadamoto et al. 'Spatiotemporally Multiresolutional Optimization Toward Supply-Demand-Storage Balancing Under PV Prediction Uncertainty'. In: *IEEE Transactions on Smart Grid* 6.2 (2015), pp. 853–865. DOI: 10.1109/TSG.2014.2377241.

[2] Yoga Sandi Perdana et al. 'Direct Connection of Supercapacitor–Battery Hybrid Storage System to the Grid-Tied Photovoltaic System'. In: *IEEE Transactions on Sustainable Energy* 10.3 (2019), pp. 1370–1379. DOI: 10.1109/TSTE.2018.2868073.

[3] Yong Liu et al. 'Frequency Response Assessment and Enhancement of the U.S. Power Grids Toward Extra-High Photovoltaic Generation Penetrations—An Industry Perspective'. In: *IEEE Transactions on Power Systems* 33.3 (2018), pp. 3438–3449. DOI: 10.1109/TPWRS.2018.2799744.

[4] Tariq Aziz and Nipon Ketjoy. 'PV Penetration Limits in Low Voltage Networks and Voltage Variations'. In: *IEEE Access* 5 (2017), pp. 16784–16792. DOI: 10.1109/ACCESS.2017.2747086.

[5] Ruifeng Yan et al. 'The Anatomy of the 2016 South Australia Blackout: A Catastrophic Event in a High Renewable Network'. In: *IEEE Transactions on Power Systems* 33.5 (2018), pp. 5374–5388. DOI: 10.1109/TPWRS.2018.2820150.

[6] Nivad Navid and Gary Rosenwald. 'Market Solutions for Managing Ramp Flexibility With High Penetration of Renewable Resource'. In: *IEEE Transactions on Sustainable Energy* 3.4 (2012), pp. 784–790. DOI: 10.1109/TSTE.2012.2203615.

[7] S. Shivashankar et al. 'Mitigating methods of power fluctuation of photovoltaic (PV) sources – A review'. In: *Renewable and Sustainable Energy Reviews* 59 (2016), pp. 1170–1184. ISSN: 1364-0321. DOI: https://doi.org/10.1016/j.rser.

2016.01.059. URL: https://www.sciencedirect.com/science/article/pii/S1364032116000897.

[8] Matthew Lave, Jan Kleissl and Ery Arias-Castro. 'High-frequency irradiance fluctuations and geographic smoothing'. In: *Solar Energy* 86.8 (2012). Progress in Solar Energy 3, pp. 2190–2199. ISSN: 0038-092X. DOI: https://doi.org/10.1016/j.solener.2011.06.031. URL: https://www.sciencedirect.com/science/article/pii/S0038092X11002611.

[9] S. Shivashankar et al. 'Mitigating methods of power fluctuation of photovoltaic (PV) sources – A review'. In: *Renewable and Sustainable Energy Reviews* 59 (2016), pp. 1170–1184. ISSN: 1364-0321. DOI: https://doi.org/10.1016/j.rser.2016.01.059. URL: https://www.sciencedirect.com/science/article/pii/S1364032116000897.

[10] Shyamal Patel, Muhammad Ahmed and Sukumar Kamalasadan. 'A Novel Energy Storage-Based Net-Load Smoothing and Shifting Architecture for High Amount of Photovoltaics Integrated Power Distribution System'. In: *IEEE Transactions on Industry Applications* 56.3 (2020), pp. 3090–3099. DOI: 10.1109/TIA.2020.2970380.

[11] Ammar Atif and Muhammad Khalid. 'Saviztky–Golay Filtering for Solar Power Smoothing and Ramp Rate Reduction Based on Controlled Battery Energy Storage'. In: *IEEE Access* 8 (2020), pp. 33806–33817. DOI: 10.1109/ACCESS.2020.2973036.

[12] Ammar Atif Abdalla et al. 'A Novel Adaptive Power Smoothing Approach for PV Power Plant with Hybrid Energy Storage System'. In: *IEEE Transactions on Sustainable Energy* 14.3 (2023), pp. 1457–1473. DOI: 10.1109/TSTE.2023.3236634.

[13] Ammar Atif Abdalla et al. 'Reliant Monotonic Charging Controllers for Parallel-Connected Battery Storage Units to Reduce PV Power Ramp Rate and Battery Aging'. In: *IEEE Transactions on Smart Grid* 14.6 (2023), pp. 4424–4438. DOI: 10.1109/TSG.2023.3250987.

[14] Viet T. Tran et al. 'Mitigation of Solar PV Intermittency Using Ramp-Rate Control of Energy Buffer Unit'. In: *IEEE Transactions on Energy Conversion* 34.1 (2019), pp. 435–445. DOI: 10.1109/TEC.2018.2875701.

[15] Kuk Yeol Bae, Han Seung Jang and Dan Keun Sung. 'Hourly Solar Irradiance Prediction Based on Support Vector Machine and Its Error Analysis'. In: *IEEE Transactions on Power Systems* 32.2 (2017), pp. 935–945. DOI: 10.1109/TPWRS.2016.2569608.

[16] Hector Beltran et al. 'Levelized Cost of Storage for Li-Ion Batteries Used in PV Power Plants for Ramp-Rate Control'. In: *IEEE Transactions on Energy Conversion* 34.1 (2019), pp. 554–561. DOI: 10.1109/TEC.2019.2891851.

[17] Hossein Dehghani Tafti et al. 'An Adaptive Control Scheme for Flexible Power Point Tracking in Photovoltaic Systems'. In: *IEEE Transactions on Power Electronics* 34.6 (2019), pp. 5451–5463. DOI: 10.1109/TPEL.2018.2869172.

[18] Efstratios I. Batzelis, Stavros A. Papathanassiou and Bikash C. Pal. 'PV System Control to Provide Active Power Reserves Under Partial Shading Conditions'. In: *IEEE Transactions on Power Electronics* 33.11 (2018), pp. 9163–9175. DOI: 10.1109/TPEL.2018.2823426.

[19] Anusha Kumaresan et al. 'Flexible Power Point Tracking for Solar Photovoltaic Systems Using Secant Method'. In: *IEEE Transactions on Power Electronics* 36.8 (2021), pp. 9419–9429. DOI: 10.1109/TPEL.2021.3049275.

[20] A.Jäger-Waldau. 'PV Status Report 2019'. In: *Publications Office of the European Union* (2019). DOI: 10.2760/326629.

[21] Hossein Dehghani Tafti et al. 'A Multi-Mode Flexible Power Point Tracking Algorithm for Photovoltaic Power Plants'. In: *IEEE Transactions on Power Electronics* 34.6 (2019), pp. 5038–5042. DOI: 10.1109/TPEL.2018.2883320.

[22] Anusha Kumaresan et al. 'Flexible Power Point Tracking for Solar Photovoltaic Systems Using Secant Method'. In: *IEEE Transactions on Power Electronics* 36.8 (2021), pp. 9419–9429. DOI: 10.1109/TPEL.2021.3049275.

[23] A. Sangwongwanich, Y. Yang and F. Blaabjerg. 'A cost-effective power ramp-rate control strategy for single-phase two-stage grid-connected photovoltaic systems'. In: (2016).

[24] Yongheng Yang et al. '6 - Flexible active power control of PV systems'. In: *Advances in Grid-Connected Photovoltaic Power Conversion Systems*. Ed. by Yongheng Yang et al. Woodhead Publishing, 2019, pp. 153–185. ISBN: 978-0-08-102339-6. DOI:

https://doi.org/10.1016/B978-0-08-102339-6.00006-3. URL: https://www.sciencedirect.com/science/article/pii/B9780081023396000063.

[25] Xingshuo Li et al. 'A cost-effective power ramp rate control strategy based on flexible power point tracking for photovoltaic system'. In: *Solar Energy* 208 (2020), pp. 1058–1067. ISSN: 0038-092X. DOI: https://doi.org/10.1016/j.solener.2020.08.044. URL: https://www.sciencedirect.com/science/article/pii/S0038092X20308859.

[26] Xingshuo Li et al. 'A Comparative Study on Photovoltaic MPPT Algorithms Under EN50530 Dynamic Test Procedure'. In: *IEEE Transactions on Power Electronics* 36.4 (2021), pp. 4153–4168. DOI: 10.1109/TPEL.2020.3024211.

[27] Gilbert M. Masters. *Renewable and Efficient Electric Power Systems*. John Wiley and Sons Inc, 2005.

[28] H. Wen et al. 'Deep Learning Based Multistep Solar Forecasting for PV Ramp-Rate Control Using Sky Images'. In: *IEEE Transactions on Industrial Informatics* 17.2 (2021), pp. 1397–1406. DOI: 10.1109/TII.2020.2987916.

[29] H. S. Jang et al. 'Solar Power Prediction Based on Satellite Images and Support Vector Machine'. In: *IEEE Transactions on Sustainable Energy* 7.3 (2016), pp. 1255–1263. DOI: 10.1109/TSTE.2016.2535466.

[30] X. Chen et al. 'Forecasting-Based Power Ramp-Rate Control Strategies for Utility-Scale PV Systems'. In: *IEEE Transactions on Industrial Electronics* 66.3 (2019), pp. 1862–1871. DOI: 10.1109/TIE.2018.2840490.

[31] T. N. Goh and K. J. Tan. 'Stochastic modeling and forecasting of solar radiation data'. In: *Solar Energy* 19.6 (1977), pp. 755–757.

[32] Gordon Reikard. 'Predicting solar radiation at high resolutions: A comparison of time series forecasts'. In: *Solar Energy* 83.3 (2009), pp. 342–349.

[33] Roberth. Shumway and Davids. Stoffer. *Time Series Analysis and Its Applications*. Springer, 2009.

[34] Neelamegam et al. 'Prediction of solar radiation for solar systems by using ANN models with different back propagation algorithms'. In: *Journal of Applied Research and Technology* (2016).

[35] Fei Wang et al. 'A day-ahead PV power forecasting method based on LSTM-RNN model and time correlation modification under partial daily pattern prediction framework'. In: *Energy Conversion and Management* 212 (2020), p. 112766. ISSN: 0196-8904. DOI: https://doi.org/10.1016/j.enconman.2020.112766. URL: https://www.sciencedirect.com/science/article/pii/S0196890420303046.

[36] K. Y. Bae, H. S. Jang and D. K. Sung. 'Hourly Solar Irradiance Prediction Based on Support Vector Machine and Its Error Analysis'. In: *IEEE Transactions on Power Systems* 32.2 (2017), pp. 935–945. DOI: 10.1109/TPWRS.2016.2569608.

[37] Junliang Fan A et al. 'Hybrid support vector machines with heuristic algorithms for prediction of daily diffuse solar radiation in air-polluted regions'. In: *Renewable Energy* 145 (2020), pp. 2034–2045.

[38] Ian Goodfellow, Yoshua Bengio and Aaron Courville. *Deep Learning*. http://www.deeplearningbook.org. MIT Press, 2016.

[39] Y. Yu, J. Cao and J. Zhu. 'An LSTM Short-Term Solar Irradiance Forecasting Under Complicated Weather Conditions'. In: *IEEE Access* 7 (2019), pp. 145651–145666. DOI: 10.1109/ACCESS.2019.2946057.

[40] M. S. Hossain and H. Mahmood. 'Short-Term Photovoltaic Power Forecasting Using an LSTM Neural Network and Synthetic Weather Forecast'. In: *IEEE Access* 8 (2020), pp. 172524–172533. DOI: 10.1109/ACCESS.2020.3024901.

[41] M. Abdel-Nasser, K. Mahmoud and M. Lehtonen. 'Reliable Solar Irradiance Forecasting Approach Based on Choquet Integral and Deep LSTMs'. In: *IEEE Transactions on Industrial Informatics* 17.3 (2021), pp. 1873–1881. DOI: 10.1109/TII.2020.2996235.

[42] X. G. Agoua, R. Girard and G. Kariniotakis. 'Short-Term Spatio-Temporal Forecasting of Photovoltaic Power Production'. In: *IEEE Transactions on Sustainable Energy* 9.2 (2018), pp. 538–546. DOI: 10.1109/TSTE.2017.2747765.

[43] X. Chen et al. 'Power ramp-rate control based on power forecasting for PV grid-tied systems with minimum energy storage'. In: *IECON 2017 - 43rd Annual Conference of the IEEE Industrial Electronics Society*. 2017, pp. 2647–2652. DOI: 10.1109/IECON.2017.8216445.

[44] Xuan Jiao et al. 'A Graph Neural Network Based Deep Learning Predictor for Spatio-Temporal Group Solar Irradiance Forecasting'. In: *IEEE Transactions on Industrial Informatics* 18.9 (2022), pp. 6142–6149. DOI: 10.1109/TII.2021.3133289.

[45] Weidong Xiao. *Photovoltaic Power System: Modeling, Design and Control*. 1st. Wiley, 2017.

[46] Zhe Song, Jia Liu and Hongxing Yang. 'Air Pollution and Soiling Implications for Solar Photovoltaic Power Generation: A Comprehensive Review'. In: *Applied Energy* 298 (2021), p. 117247. ISSN: 0306-2619. DOI: https://doi.org/10.1016/j.apenergy.2021.117247. URL: https://www.sciencedirect.com/science/article/pii/S030626192100667X.

[47] Benyounes Raillani et al. 'A New Proposed Method to Mitigate the Soiling Rate of a Photovoltaic Array Using First-Row Height'. In: *Applied Energy* 331 (2023), p. 120403. ISSN: 0306-2619. DOI: https://doi.org/10.1016/j.apenergy.2022.120403.

[48] Yechen Zhu and Weidong Xiao. 'A comprehensive review of topologies for photovoltaic I–V curve tracer'. In: *Solar Energy* 196 (2020), pp. 346–357. DOI: 10.1016/j.solener.2019.12.020.

[49] Md. Mahamudul Hasan Mithhu, Tahmina Ahmed Rima and M. Ryyan Khan. 'Global Analysis of Optimal Cleaning Cycle and Profit of Soiling Affected Solar Panels'. In: *Applied Energy* 285 (2021), p. 116436. ISSN: 0306-2619. DOI: https://doi.org/10.1016/j.apenergy.2021.116436. URL: https://www.sciencedirect.com/science/article/pii/S0306261921000039.

[50] Pramod Nepal et al. 'Accurate Soiling Ratio Determination With Incident Angle Modifier for PV Modules'. In: *IEEE Journal of Photovoltaics* 9.1 (2019), pp. 295–301. DOI: 10.1109/JPHOTOV.2018.2882468.

[51] Suellen C. S. Costa, Lawrence L. Kazmerski and Antonia Sônia A. C. Diniz. 'Estimate of Soiling Rates Based on Soiling Monitoring Station and PV System Data: Case Study for Equatorial-Climate Brazil'. In: *IEEE Journal of Photovoltaics* 11.2 (2021), pp. 461–468. DOI: 10.1109/JPHOTOV.2020.3047187.

[52] Matthew Muller et al. 'An In-depth Field Validation of "DUSST": a Novel Low-maintenance Soiling Measurement Device'. In: *Progress in Photovoltaics: Research and Applications* 29.8 (2021), pp. 953–967.

[53] Olga Kalashnikova Stewart Isaacs et al. 'Dust Soiling Effects on Decentralized Solar in West Africa'. In: *Applied Energy* 340 (2023), p. 120993. DOI: https://doi.org/10.1016/j.apenergy.2023.120993.

[54] Oystein Ovrum et al. 'Comparative Analysis of Site-Specific Soiling Losses on PV Power Production'. In: *IEEE Journal of Photovoltaics* 11.1 (2021), pp. 158–163. DOI: 10.1109/JPHOTOV.2020.3032906.

[55] Klemens Ilse et al. 'Dew as a Detrimental Influencing Factor for Soiling of PV Modules'. In: *IEEE Journal of Photovoltaics* 9.1 (2019), pp. 287–294. DOI: 10.1109/JPHOTOV.2018.2882649.

[56] R. Muhammad Ehsan et al. 'Effect of Soiling on Photovoltaic Modules and Its Mitigation Using Hydrophobic Nanocoatings'. In: *IEEE Journal of Photovoltaics* 11.3 (2021), pp. 742–749. DOI: 10.1109/JPHOTOV.2021.3062023.

[57] Benyounes Raillani et al. 'A New Proposed Method to Mitigate the Soiling Rate of a Photovoltaic Array Using First-row Height'. In: *Applied Energy* 331 (2023), p. 120403. ISSN: 0306-2619. DOI: https://doi.org/10.1016/j.apenergy.2022.120403. URL: https://www.sciencedirect.com/science/article/pii/S0306261922016609.

[58] Leonardo Micheli et al. 'Extracting and Generating PV Soiling Profiles for Analysis, Forecasting, and Cleaning Optimization'. In: *IEEE Journal of Photovoltaics* 10.1 (2020), pp. 197–205. DOI: 10.1109/JPHOTOV.2019.2943706.

[59] Wan Juzaili Jamil et al. 'Modeling of Soiling Derating Factor in Determining Photovoltaic Outputs'. In: *IEEE Journal of Photovoltaics* 10.5 (2020), pp. 1417–1423. DOI: 10.1109/JPHOTOV.2020.3003815.

[60] Åsmund Skomedal and Michael G. Deceglie. 'Combined Estimation of Degradation and Soiling Losses in Photovoltaic Systems'. In: *IEEE Journal of Photovoltaics* 10.6 (2020), pp. 1788–1796. DOI: 10.1109/JPHOTOV.2020.3018219.

[61] Mingda Yang, Jim Ji and Bing Guo. 'Soiling Quantification Using an Image-Based Method: Effects of Imaging Conditions'. In: *IEEE Journal of Photovoltaics* 10.6 (2020), pp. 1780–1787. DOI: 10.1109/JPHOTOV.2020.3018257.

[62] Bernd Doll et al. 'Luminescence Analysis of PV-Module Soiling in Germany'. In: *IEEE Journal of Photovoltaics* 12.1 (2022), pp. 81–87. DOI: 10.1109/JPHOTOV.2021.3123076.

[63] Sachin Mehta et al. 'DeepSolarEye: Power Loss Prediction and Weakly Supervised Soiling Localization via Fully Convolutional Networks for Solar Panels'. In: *2018 IEEE Winter Conference on Applications of Computer Vision (WACV)*. 2018, pp. 333–342. DOI: 10.1109/WACV.2018.00043.

[64] Robinson Cavieres et al. 'Automatic Soiling and Partial Shading Assessment on PV Modules through RGB Images Analysis'. In: *Applied Energy* 306 (2022), p. 117964.

[65] Yifeng Chen et al. 'From Laboratory to Production: Learning Models of Efficiency and Manufacturing Cost of Industrial Crystalline Silicon and Thin-Film Photovoltaic Technologies'. In: *IEEE Journal of Photovoltaics* 8.6 (2018), pp. 1531–1538. DOI: 10.1109/JPHOTOV.2018.2871858.

[66] S.K. Firth, K.J. Lomas and S.J. Rees. 'A simple model of PV system performance and its use in fault detection'. In: *Solar Energy* 84.4 (2010). International Conference CISBAT 2007, pp. 624–635. ISSN: 0038-092X. DOI: https://doi.org/10.1016/j.solener.2009.08.004.

[67] Dhanup S. Pillai and N. Rajasekar. 'A comprehensive review on protection challenges and fault diagnosis in PV systems'. In: *Renewable and Sustainable Energy Reviews* 91 (2018), pp. 18–40. ISSN: 1364-0321. DOI: https://doi.org/10.1016/j.rser.2018.03.082.

[68] Yihua Hu et al. 'Online Two-Section PV Array Fault Diagnosis With Optimized Voltage Sensor Locations'. In: *IEEE Transactions on Industrial Electronics* 62.11 (2015), pp. 7237–7246. DOI: 10.1109/TIE.2015.2448066.

[69] Palak Jain et al. 'A Digital Twin Approach for Fault Diagnosis in Distributed Photovoltaic Systems'. In: *IEEE Transactions on Power Electronics* 35.1 (2020), pp. 940–956. DOI: 10.1109/TPEL.2019.2911594.

[70] Khaled A. Saleh et al. 'Voltage-Based Protection Scheme for Faults Within Utility-Scale Photovoltaic Arrays'. In: *IEEE Transactions on Smart Grid* 9.5 (2018), pp. 4367–4382. DOI: 10.1109/TSG.2017.2655444.

[71] Chenxi Li et al. 'A fast MPPT-based anomaly detection and accurate fault diagnosis technique for PV arrays'. In: *Energy Conversion and Management* 234 (2021), p. 113950. ISSN: 0196-8904. DOI: https://doi.org/10.1016/j.enconman.2021.113950.

[72] Sourov Roy et al. 'An Irradiance-Independent, Robust Ground-Fault Detection Scheme for PV Arrays Based on Spread Spectrum Time-Domain Reflectometry (SSTDR)'. In: *IEEE Transactions on Power Electronics* 33.8 (2018), pp. 7046–7057. DOI: 10.1109/TPEL.2017.2755592.

[73] Mohammed Khorshed Alam et al. 'PV ground-fault detection using spread spectrum time domain reflectometry (SSTDR)'. In: *2013 IEEE Energy Conversion Congress and Exposition*. 2013, pp. 1015–102. DOI: 10.1109/ECCE.2013.6646814.

[74] Tingting Pei et al. 'Module block fault locating strategy for large-scale photovoltaic arrays'. In: *Energy Conversion and Management* 214 (2020), p. 112898. ISSN: 0196-8904. DOI: https://doi.org/10.1016/j.enconman.2020.112898.

[75] Pradeep Kumar Boggarapu et al. 'Identification of Pre-existing/Undetected Line-to-Line Faults in PV Array Based on Preturn on/off Condition of the PV Inverter'. In: *IEEE Transactions on Power Electronics* 35.11 (2020), pp. 11865–11878. DOI: 10.1109/TPEL.2020.2987856.

[76] Wenguan Wang et al. 'Fault Diagnosis of Photovoltaic Panels Using Dynamic Current–Voltage Characteristics'. In: *IEEE Transactions on Power Electronics* 31.2 (2016), pp. 1588–1599. DOI: 10.1109/TPEL.2015.2424079.

[77] Chenxi Li et al. 'A fast MPPT-based anomaly detection and accurate fault diagnosis technique for PV arrays'. In: *Energy Conversion and Management* 234 (2021), p. 113950.

ISSN: 0196-8904. DOI: https://doi.org/10.1016/j.enconman.2021.113950.

[78] Indra Man Karmacharya and Ramakrishna Gokaraju. 'Fault Location in Ungrounded Photovoltaic System Using Wavelets and ANN'. In: *IEEE Transactions on Power Delivery* 33.2 (2018), pp. 549–559. DOI: 10.1109/TPWRD.2017.2721903.

[79] Zhicong Chen et al. 'Deep residual network based fault detection and diagnosis of photovoltaic arrays using current-voltage curves and ambient conditions'. In: *Energy Conversion and Management* 198 (2019), p. 111793. ISSN: 0196-8904. DOI: https://doi.org/10.1016/j.enconman.2019.111793.

[80] Ye Zhao et al. 'Graph-Based Semi-supervised Learning for Fault Detection and Classification in Solar Photovoltaic Arrays'. In: *IEEE Transactions on Power Electronics* 30.5 (2015), pp. 2848–2858. DOI: 10.1109/TPEL.2014.2364203.

[81] Zhehan Yi and Amir H. Etemadi. 'Line-to-Line Fault Detection for Photovoltaic Arrays Based on Multiresolution Signal Decomposition and Two-Stage Support Vector Machine'. In: *IEEE Transactions on Industrial Electronics* 64.11 (2017), pp. 8546–8556. DOI: 10.1109/TIE.2017.2703681.

[82] Fouzi Harrou et al. 'An unsupervised monitoring procedure for detecting anomalies in photovoltaic systems using a one-class Support Vector Machine'. In: *Solar Energy* 179 (2019), pp. 48–58. ISSN: 0038-092X. DOI: https://doi.org/10.1016/j.solener.2018.12.045.

[83] Leian Chen, Shang Li and Xiaodong Wang. 'Quickest Fault Detection in Photovoltaic Systems'. In: *IEEE Transactions on Smart Grid* 9.3 (2018), pp. 1835–1847. DOI: 10.1109/TSG.2016.2601082.

[84] Ye Zhao et al. 'Outlier detection rules for fault detection in solar photovoltaic arrays'. In: *2013 Twenty-Eighth Annual IEEE Applied Power Electronics Conference and Exposition (APEC)*. 2013, pp. 2913–2920. DOI: 10.1109/APEC.2013.6520712.

[85] Fouzi Harrou, Bilal Taghezouit and Ying Sun. 'Improved kNN-Based Monitoring Schemes for Detecting Faults in PV Systems'. In: *IEEE Journal of Photovoltaics* 9.3 (2019), pp. 811–821. DOI: 10.1109/JPHOTOV.2019.2896652.

[86] Zhehan Yi and Amir H. Etemadi. 'Fault Detection for Photovoltaic Systems Based on Multi-Resolution Signal Decomposition and Fuzzy Inference Systems'. In: *IEEE Transactions on Smart Grid* 8.3 (2017), pp. 1274–1283. DOI: 10.1109/TSG.2016.2587244.

[87] Dhanup S. Pillai and N. Rajasekar. 'An MPPT-Based Sensorless Line–Line and Line–Ground Fault Detection Technique for PV Systems'. In: *IEEE Transactions on Power Electronics* 34.9 (2019), pp. 8646–8659. DOI: 10.1109/TPEL.2018.2884292.

[88] Holger Ruf. 'Limitations for the feed-in power of residential photovoltaic systems in Germany – An overview of the regulatory framework'. In: *Solar Energy* 159 (2018), pp. 588–600.

[89] Gordon Reikard. 'Predicting solar radiation at high resolutions: A comparison of time series forecasts'. In: *Solar Energy* 83.3 (2009), pp. 342–349.

[90] K. Y. Bae, H. S. Jang and D. K. Sung. 'Hourly Solar Irradiance Prediction Based on Support Vector Machine and Its Error Analysis'. In: *IEEE Transactions on Power Systems* 32.2 (2017), pp. 935–945. DOI: 10.1109/TPWRS.2016.2569608.

[91] Sahbi Boubaker et al. 'Deep Neural Networks for Predicting Solar Radiation at Hail Region, Saudi Arabia'. In: *IEEE Access* 9 (2021), pp. 36719–36729. DOI: 10.1109/ACCESS.2021.3062205.

[92] Wei Liu and Yozo Shoji. 'DeepVM: RNN-Based Vehicle Mobility Prediction to Support Intelligent Vehicle Applications'. In: *IEEE Transactions on Industrial Informatics* 16.6 (2020), pp. 3997–4006. DOI: 10.1109/TII.2019.2936507.

[93] Yunjun Yu, Junfei Cao and Jianyong Zhu. 'An LSTM Short-Term Solar Irradiance Forecasting Under Complicated Weather Conditions'. In: *IEEE Access* 7 (2019), pp. 145651–145666. DOI: 10.1109/ACCESS.2019.2946057.

[94] Chukwan Siridhipakul and Peerapon Vateekul. 'Multi-step Power Consumption Forecasting in Thailand Using Dual-Stage Attentional LSTM'. In: (2019), pp. 1–6. DOI: 10.1109/ICITEED.2019.8929966.

[95] Amirhossein Dolatabadi, Hussein Abdeltawab and Yasser Abdel-Rady I. Mohamed. 'Deep Spatial-Temporal 2-D CNN-BLSTM Model for Ultrashort-Term LiDAR-Assisted

Wind Turbine's Power and Fatigue Load Forecasting'. In: *IEEE Transactions on Industrial Informatics* 18.4 (2022), pp. 2342–2353. DOI: 10.1109/TII.2021.3097716.

[96] Efstratios I. Batzelis, Georgios E. Kampitsis and Stavros A. Papathanassiou. 'Power Reserves Control for PV Systems With Real-Time MPP Estimation via Curve Fitting'. In: *IEEE Trans Sustain Energy* 8.3 (2017), pp. 1269–1280. DOI: 10.1109/TSTE.2017.2674693.

[97] R. Hariharan et al. 'A Method to Detect Photovoltaic Array Faults and Partial Shading in PV Systems'. In: *IEEE Journal of Photovoltaics* 6.5 (2016), pp. 1278–1285. DOI: 10.1109/JPHOTOV.2016.2581478.